QATAR UNIVERSITY

COLLEGE OF ENGINEERING

HIGH-POWER MULTIPORT DC-DC CONVERTER FOR PV FARM APPLICATIONS

BY

MOHAMMAD KHODADADY

A Thesis Submitted to

the Faculty of the College of Engineering

in Partial Fulfillment of the Requirements for the Degree of

Master of Science in Electrical Engineering

June 2019

COMMITTEE PAGE

The members of the Committee approve the Thesis of Mohammad
Khodadady defended on 17/04/2019.

_____
Nader Meskin
Thesis/Dissertation Supervisor

_____
Ahmed Massoud
Thesis/Dissertation Supervisor

_____
Atif Iqbal
Committee Member

_____
Shady Gadoue
Committee Member

Approved:

_____
Abdel Magid Hamouda, Dean, College of Engineering

ABSTRACT

Khodadady, Mohammad, N., Masters : June : 2019, Master of Science in Electrical Engineering

Title: High-power Multiport DC-DC Converter for PV Farm Applications

Supervisor of Thesis: Nader M. Meskin and Ahmed M. Masoud

The trend toward generating electricity from renewable energy sources has encouraged researchers to work on finding more reliable and efficient ways of combining various sources, storage systems, and loads with different voltage ratings. Using the conventional structure of integrating multiple sources is proven to be less efficient and more expensive. This has led to the development of the multiport DC-DC converter, which provides a localized energy processing model with a centralized controller. This research studies the operation and characteristics of the multiport DC-DC converter, specifically for medium-voltage and high-power applications. The steady state and the dynamical modeling of the multiport DC-DC converter are presented in this work. A mathematical representation of the average current model is derived, and it is used to obtain the linearized model of the multiport DC-DC converter. Non-Overshooting state feedback controller is designed and implemented for a five-port converter, and its performance is compared with the conventional optimal control scheme. In addition, fault analysis is carried out by studying the system response under different fault scenarios and evaluating the controller's ability to adjust the power flow between the ports.

DEDICATION

This work is dedicated to my beloved family.

ACKNOWLEDGMENTS

I would like to express my gratitude to my supervisors Dr. Nader Meskin and Dr. Ahmed Massoud for their guidance, support, and encouragement throughout my master's thesis. Their guidance was a crucial asset that helped me to finish my thesis. I would like to thank my family for their continuous support and encouragement.

TABLE OF CONTENTS

LIST OF TABLES

LIST OF FIGURES

LIST OF ABBREVIATIONS

AVM	Average Value Model
BESS	Battery Energy Storage System
DAB	Dual Active Bridge
KCL	Kirchhoff's Current Law
LQR	Linear Quadratic Regulator
LSM	Large Signal Model
MIMO	Multi-Input Multi-Output
PI	Proportional-Integral
PID	Proportional-Integral-Derivative
PWM	Pulse Width Modulation
SISO	Single-Input Single-Output
SSM	Small Signal Model
TAB	Triple Active Bridge
UG	Utility Grid
ZVS	Zero Voltage Switching

CHAPTER 1: INTRODUCTION

Generating electricity from renewable energy sources such as photovoltaic (PV), fuel cell, and wind has gained great attention in the past decade. This is mainly due to the environmental impact and non-renewable nature of fossil fuel based energy sources such as coal, oil, and natural gas. Climate change is currently a major topic, and it has raised more attention from different organizations and countries on the impact of fossil fuel. In addition, the energy demand is constantly increasing due to industrial and population growth. It is projected that world energy consumption will increase by 28% between 2015 and 2040 [1]. Although the environmental impact of fossil fuel is non-negligible, it remains to be the main source for generating electricity in many countries, and it accounts for 78% of the global energy production according to the latest report from Renewable Energy Policy Network for the 21st Century (REN21) [2]. However, there has been a steady increase in generating energy from different energy sources in the past decade. It was estimated that in 2015, almost 1,800 gigawatt (GW) of global energy was generated from renewable energy [2]. This number is increased by 9% in 2016. Moreover, the annual capacity of added renewable energy is more than all fossil fuels combined [2]. Figure 1 illustrates the power capacity of renewable energy sources in the top six countries in generating electricity from renewable energy sources. Solar PV, for the first time, has accounted for the highest installed energy source of all power generation technologies. This increase is driven by the decline in the prices of PV technology, and it is expected that the prices will decline more in the future.
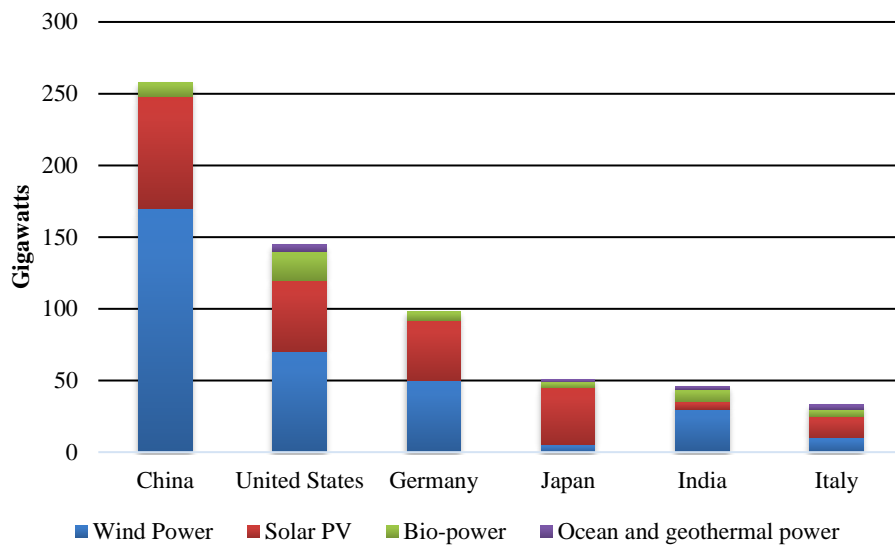
Figure 1. Renewable power capacity in the top six countries.

Although the price of PV technology is declining every year, it is still relatively more expansive than fossil fuel. This has forced the investors and designers to look for extracting the maximum output from the installed PV. Generating high capacity from PV not only requires a careful selection of the geographical parameters but also in the electrical infrastructure, which plays an important role in the PV system design [3].

One of the main components in the electrical infrastructure of the PV system is the DC-DC converter. Figure 2 shows a typical power electronic circuit for a PV system which consists of an energy source (PV), a converter to extract the maximum power, a controller to control the operation of the converter by taking the measurements from the source and the load, and finally the load.
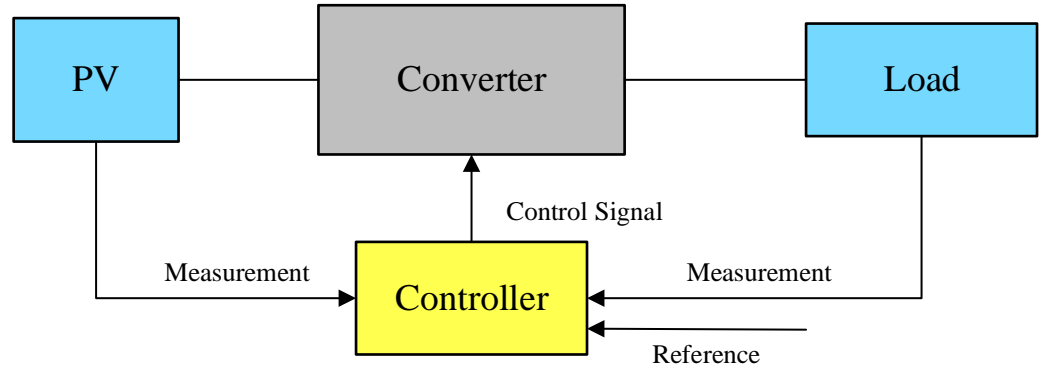
Figure 2. Power conversion in a PV system.

The above structure is mainly suitable for applications where there are only one energy source and a single load. For large PV systems, there are multiple PV parks located in different locations. In addition, PV can only supply energy when there is sunlight, so it is essential to have an energy storage device to store the excess energy and supply the loads during the night time. As a result, it is important to have a converter with multiple inputs and output to integrate the energy supply from multiple PV parks and store this energy in storage devices or supply it to the load. Such systems can be structured as shown in Figure 3. This conventional method of integrating multiple sources is constructed by connecting all the renewable energy sources to a common high-/low-voltage DC bus. Several types of converters have been developed, which can be used in such systems such as fly-back converter [4], push-pull converter [5], phase-shifted full-bridge converter [6], etc. This structure for combining renewable energy sources has several disadvantages. First, each source requires a separate converter resulting in a large number of components, larger weight, and higher cost. Another disadvantage of such configuration is related to controlling the power flow through the converters. Each converter is controlled

3

individually without considering the performance of the overall system. These drawbacks can have a significant impact on the efficiency of the PV system.
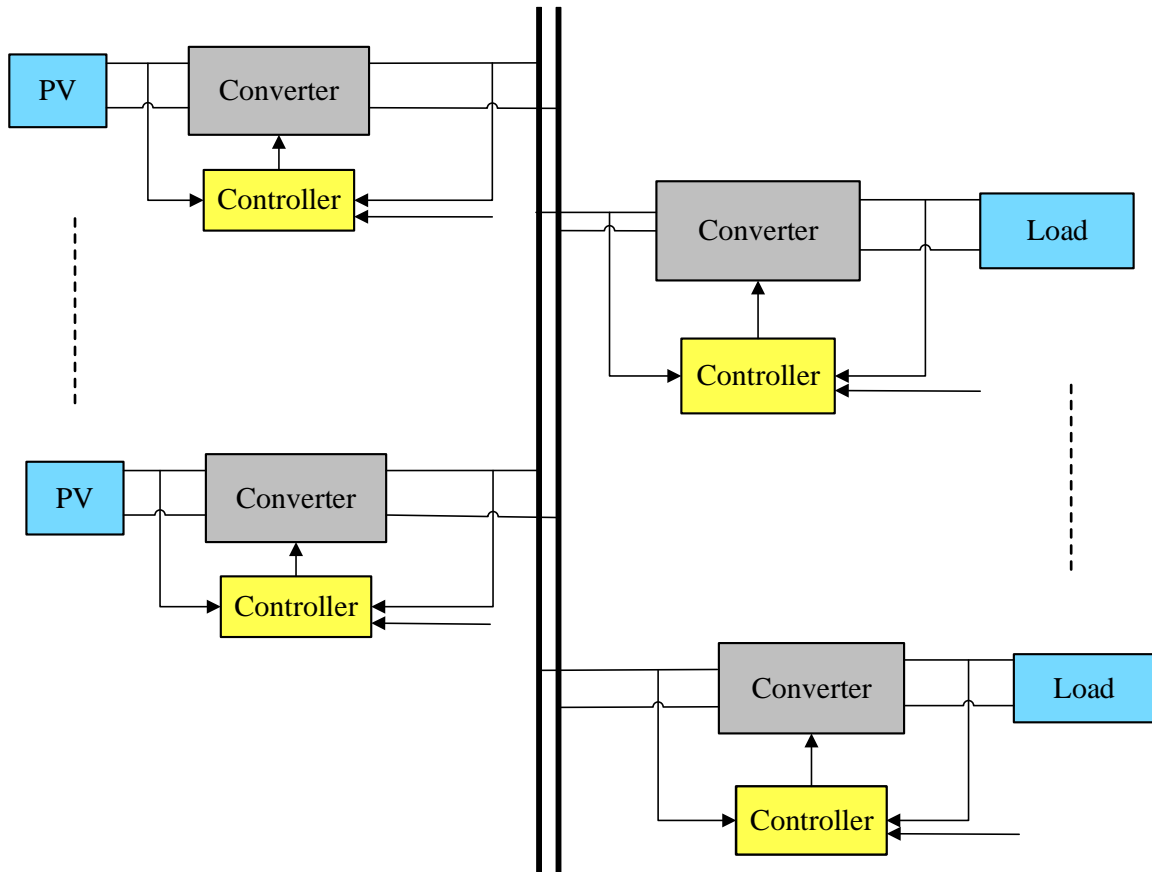
Figure 3. Conventional structure of integrating multiple sources.

Another way of integrating multiple DC-sources is by using multiport converters [7], which overcome many of the disadvantages of the conventional structure. Figure 4 illustrates the structure of a multiport converter. All the PV sources are connected to a single converter, which helps to reduce the weight and the cost significantly. In addition, this topology allows all sources and loads of different voltages to be connected to the same

converter as opposed to the conventional structure. Moreover, a single controller is used to adjust the power flow between the ports, the storage system, and the loads. Some topologies of multiport converter have transformers for providing galvanic isolation for safety in high voltage applications. The reduction in the number of active switches and improved control strategy in this structure can enhance the efficiency of the system greatly compared to the conventional structure [7].
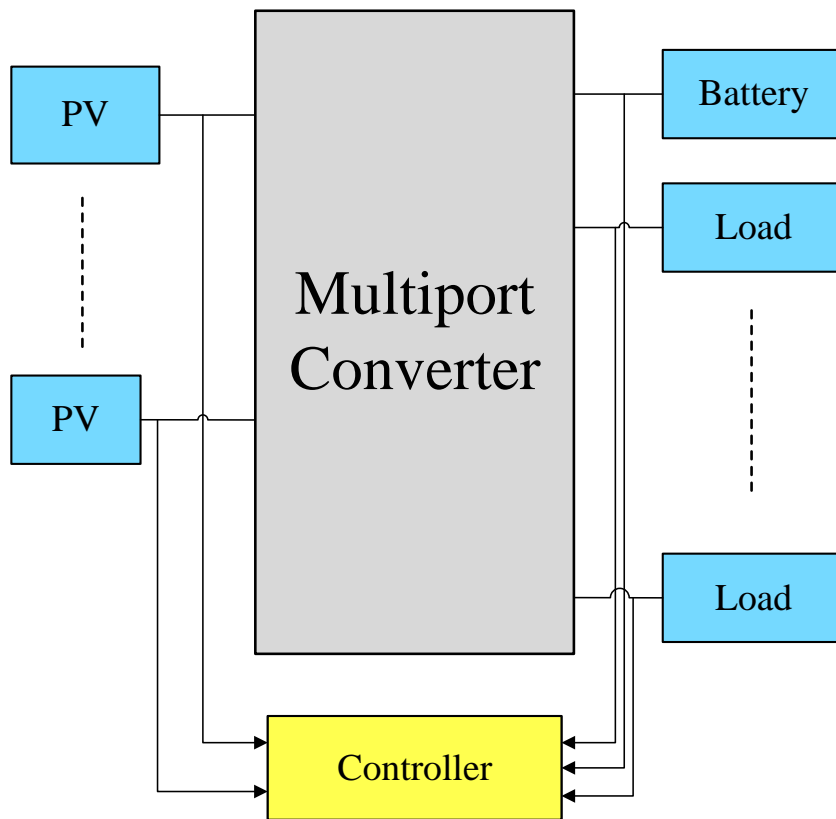
Figure 4. Multiport DC-DC Converter.

Having multiple sources and loads connected to the same converter makes dealing with faults more challenging. A reliable multiport system must be able to prevent the fault

from propagating to other parts of the network by isolating the faulted port. Moreover, a suitable control strategy must be adopted to minimize the impact of faults on the converter by adjusting the power flow between the ports.

1.1 Overview of Previous Work

There are two main categories of multiport converters: isolated and non-isolated converters. In the isolated multiport converter, a transformer is added between the sources and the loads to provide galvanic isolation. Based on the topology of the converter, flux addition using multi-winding transformer [8], DC-link method [9], or time-sharing concept [10] is applied to transfer energy from the primary side of the transformer to the secondary side. On the other hand, the non-isolated multiport converter is an inexpensive solution compared to the isolated converter topology. It requires less components, and it is smaller in size, which makes it more suitable for low-cost applications.

1.1.1 Non-Isolated Multiport Converter

The dual input buck/buck-boost converter presented in [11] consists of a low-voltage port, high-voltage port, and an output port. Conventional Pulse Width Modulation (PWM) is used to control the switches to allow power flow to be controlled either separately or simultaneously. Soft switching is accessible in this topology. A switched-capacitor based multi-input summation converter is presented in [12] which consists of N number of capacitors and active switches, where N is the number of input sources. This converter requires a large output capacitor to minimize the ripple. In order to achieve soft-switching, a small resonant inductor is connected in series with each switched-capacitor, and the switching frequency is set to be lower than the resonant frequency. The converter in [13] is derived from the traditional boost converter with an auxiliary circuit. The

auxiliary circuit is constructed by connecting a small inductor in series with a diode and a switch connected in series with a capacitor. The purpose of this circuit is to achieve turn-on Zero Voltage Switching (ZVS) for all switches and to eliminate the large reverse recovery current of the output diode. The unidirectional multi-input multi-output converter in [14] has a single inductor to transfer the energy between the sources and the load. The use of single inductor can help to decrease the size and cost of the converter, and current sensing can be done more easily. Duty cycle control is optimized to control the switching legs in this topology.

1.1.2 Isolated Multiport Converter

A new family of multi-input converters is introduced in [15], which combines both DC link and magnetic coupling. Two types of multiport converters were introduced, half-bridge and full-bridge converter. In the half-bridge converters, a DC bus is used to link both the input half-bridge circuits, and an isolation transformer is implemented to link the inputs with the load. This topology integrates a bidirectional buck/boost topology and bidirectional boost dual half-bridge. In addition to providing isolation, the transformer in this topology is also used to boost the low dc-link voltage. The full-bridge converter integrates two-phase boost units [16]. The power flow in the boost units is controlled by utilizing the duty cycle of the switches, and the power flow through the load is controlled by adjusting the phase shift between the legs. The primary side ports in this topology are bidirectional. The load port can also be bidirectional if the synchronous rectification is applied and unidirectional if diode rectifiers are employed.

All the multiport converters introduced above are most suitable for low/medium voltage applications. For high-power high-voltage applications, the most suitable topology

is the Dual Active Bridge (DAB) [17], which forms a building block for different high-power multiport converters.

Figure 5 shows a two-input current-fed converter which transfers the input energy from multiple sources through the multi-winding transformer [8]. The magnetic flux produced by each winding is added-up in the coupled magnetic core of the transformer to combine the energy produced by each current source. The four diodes at the output side are used for rectification. This topology is capable of transferring energy from sources with different voltage levels by converting the voltage source to current sources using Choke inductor. To prevent reverse current flow from the sources and allow the operation of both DC sources simultaneously, the reverse blocking diodes are integrated into the input stage. The control of the active switches is done by utilizing phase shifted PWM which helps to prevent voltage clamping in the transformer's windings and to provide soft-switching operation. This topology is capable of only delivering the energy in one direction, which makes it unsuitable in applications where the energy storage system is implemented.
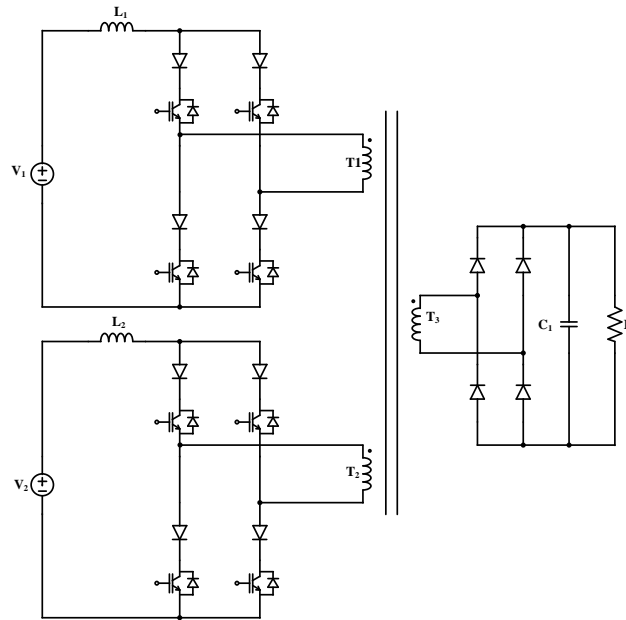
Figure 5. Two-input current-fed full-bridge converter.

The topology shown in Figure 6 is based on series resonant where each full-bridge unit is connected to a transformer winding through a series resonant circuit [18]. The output voltage is controlled by adjusting the phase shift angle between the output voltage of each full bridge unit, and the direction of power flow is controlled by adjusting the phase shift between the pairs of active switches. Soft switching is only achieved when the converter is operating above the resonant frequency. Some drawbacks of this topology that it requires large resonant inductors and capacitors, and variable frequency control to maintain soft switching.
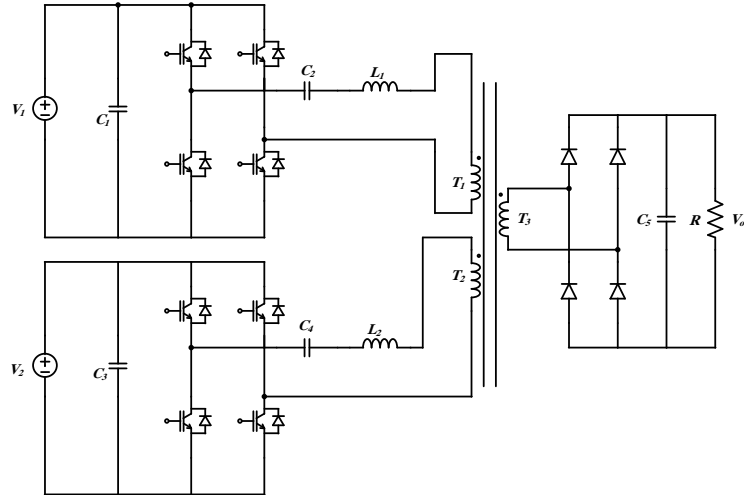
Figure 6. Series resonant DC-DC converter.

The Triple Active Bridge (TAB) converter shown in Figure 7 is just an expansion of the DAB, and it is capable of providing bidirectional power which makes it suitable for energy storage applications [19]. Using the conventional phase-shifted PWM allows ZVS for a small range of voltage level. Due to the large variation in the voltage level specifically when connecting one of the ports to supercapacitors for energy storage or when snubber capacitors are added in parallel to the switches, soft switching has to be guaranteed through the whole operations range. By applying duty cycle control to the TAB topology, it is possible to achieve soft switching ZVS over the complete range. In addition, two PI feedback loops are used to achieve constant voltage and constant power.
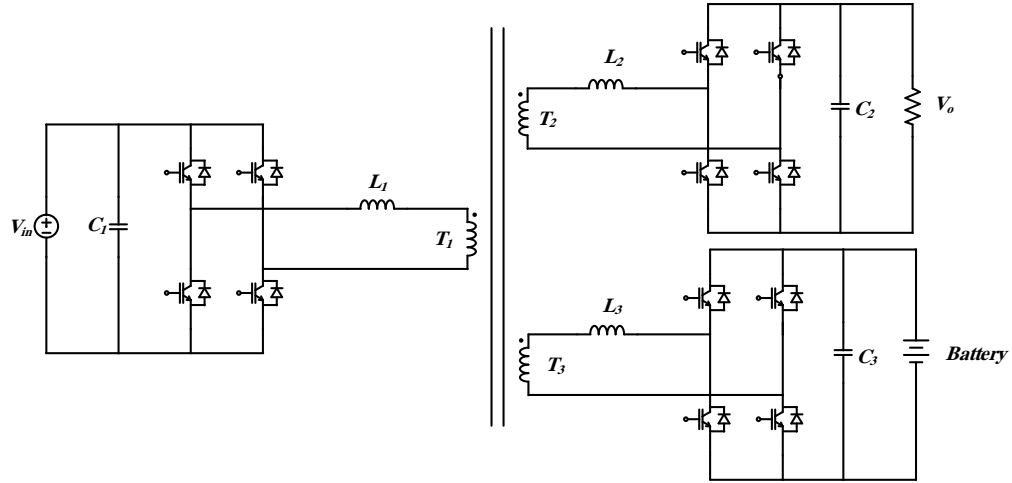
Figure 7. Triple active bridge bidirectional converter.

1.2 Research Challenges

Extensive research works have been done in designing multiport converters. However, the proposed topologies in the literature have one or more of the following disadvantages:

1- The main focus of the past literature has been toward the design of the circuit without considering enhancing the stability of the system under different operation modes.

2- Mostly conventional controllers such as PID controller are used.

3- Lack of bidirectional supply capability between all ports.

4- Applied to low power applications.

5- The dynamic response of the system under load change while keeping constant voltage is not well studied.

The TAB converter illustrated in Figure 7 can be further extended to an N-port converter. In addition, it supports bidirectional power flow and can be applied in high-power applications. These properties make this topology an attractive option for high-power multiport converter for renewable energy systems. More advanced control systems can be applied in order to enhance the voltage and current response of the system under load change.

1.3 Thesis Objectives and Contributions

The objective of this thesis is to design and implement a non-overshooting control structure for a DAB based multiport converter for medium-voltage and high-power applications with bidirectional power flow capability. The thesis will include analysis, modeling, and simulation of the multiport converter. An improved closed-loop controller will be developed to manage the power flow between the energy sources, storage devices, and loads while maintaining a constant voltage. Simulation of the multiport converter under different operation modes will be analyzed to evaluate the performance of the controller. The case study that will be analyzed in this thesis is illustrated in Figure 8 which consists of a Utility Grid (UG), Battery Energy Storage System (BESS) to store the excess energy and to supply the UG when power is needed, and three Photovoltaic (PV) ports that supply the UG and BESS. In the medium-voltage multiport converter under-study, the voltage of the UG is rated at 11kV, whereas the voltage of the BESS is rated at 2 kV and each PV farm can supply 1.5kV. The PV voltage selected based on the maximum allowed voltage for the high-voltage PV system according to the National Electric Code [20]. Each port can supply up to 0.5 MW.

The main contribution of the thesis can be summarized as follows:

- Analyze and model medium-voltage high-power multiport DC-DC converter.

- Develop a non-overshooting controller capable of eliminating the overshoot from voltage and current response.

- Compare the system response under optimal and non-overshooting control schemes.

- Assess the system's response to fault.
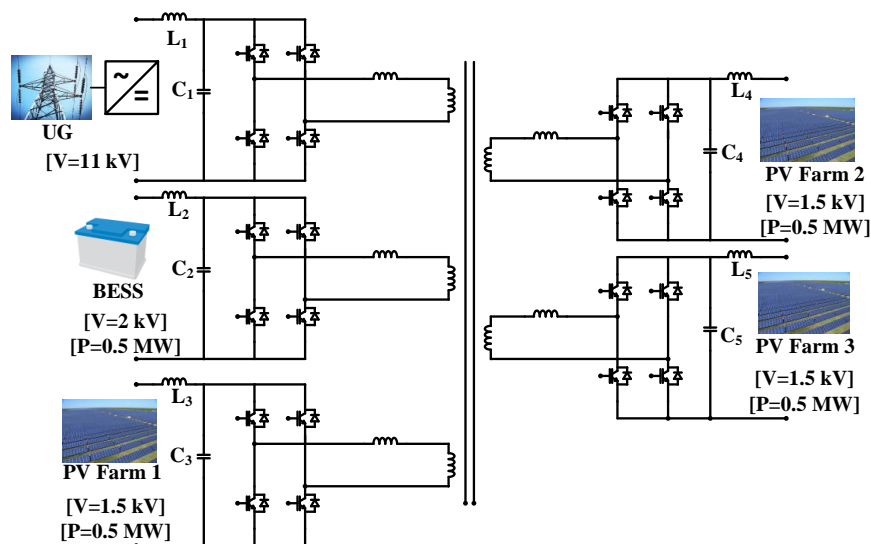
Figure 8. Multiport DC-DC converter.

1.4 Thesis Structure

This thesis is organized as follows:

Chapter 1 includes the problem statement of the importance of renewable energy and the challenges in integrating multiple renewable energy sources and storage system with the grid. In addition, a literature review is conducted on the development of multiport DC-DC

converter. Several topologies are presented along with their operation, application, and drawbacks. Finally, in this chapter, the research challenges and the objectives of the thesis are defined. Chapter 2 presents the characteristics of DAB converter and its average waveforms. The average power and current equations of the DAB are derived. The DAB is extended to the multiport converter, and the average value model is obtained by deriving the large and small signal model of each port. The detailed model which contains the non-linear characteristics of the multiport converter is presented as well. Moreover, the input/output filter design of the multiport converter is studied to minimize voltage and current ripples. Chapter 3 presents the control structure of the converter and analysis of the response of the system using two controllers. Chapter 4 includes a summarization of the major contributions of this research and the recommendations for future work.

CHAPTER 2: MULTIPORT CONVERTER MODELING

This chapter demonstrates the operation principle of the multiport converter using the averaging method. The average power equation is first derived for the dual active bridge converter and used to find the average current. The next section studies the modeling of the multi-winding transformer that will be implemented in the multiport converter. A simulation is carried out for the multi-winding transformer to represent the power transfer between the ports. Next, using the averaging current equation of the DAB, the large signal, small signal, and detailed models of the multiport converter are obtained. Finally, the equations for calculating the minimum LC filter value is derived.

2.1 Dual Active Bridge

The DAB converter illustrated in Figure 9 is used to demonstrate the averaging method which will be applied for the multiport structure. The converter consists of two H-bridges coupled by a high-frequency transformer. The intermediate transformer provides galvanic isolation and prevents common-mode current [21]. The DAB can be designed as single-phase or three-phase depending on the design requirements. In the multiport system under-study, a single-phase DAB is used to analyze the multiport system in order to simplify the analysis. Both single-phase and three-phase systems can be used in the medium-voltage multiport system since the main objective of the AC link is only to provide galvanic isolation. The simplified model of the DAB primary referred circuit is presented in Figure 10. The transformer's winding is represented by a leakage inductor L. The voltage across the inductor is the difference between the two square wave voltages $v_1(t)$ and $v_2(t)$.
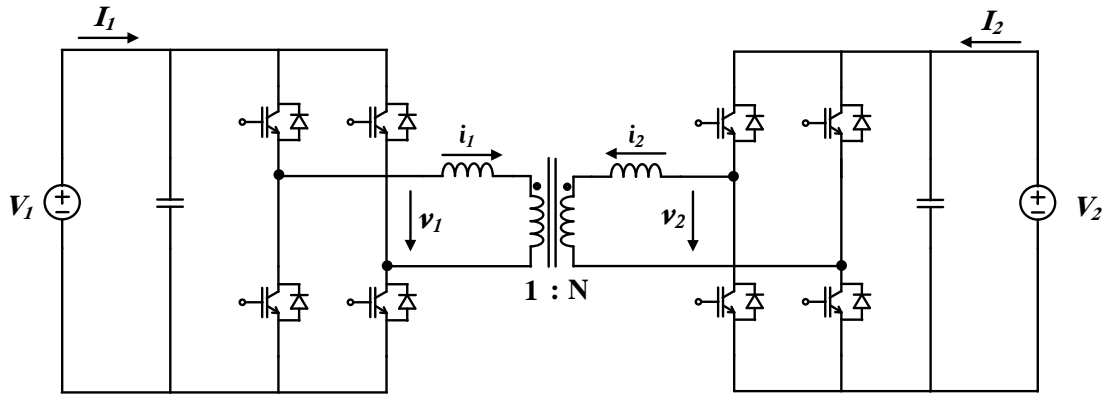
Figure 9. DAB converter circuit.
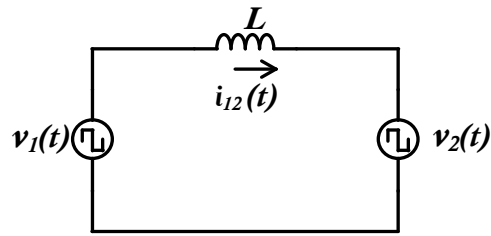
Figure 10. Equivalent circuit of DAB.

Figure 11 shows the operating waveform of DAB in case of power transfer from $v_1(t)$ to $v_2(t)$. Both $v_1(t)$ and $v_2(t)$ are a square wave with 50% duty cycle. The phase shift of the pulses between the full bridges defines the power flow direction between the ports, and it is denoted by ϕ. The inductor leakage current $i_{12}(t)$ is a function of $\theta(t) = \omega t$ where ω is the switching frequency [22]. I_1 and I_2 represent the port's current.
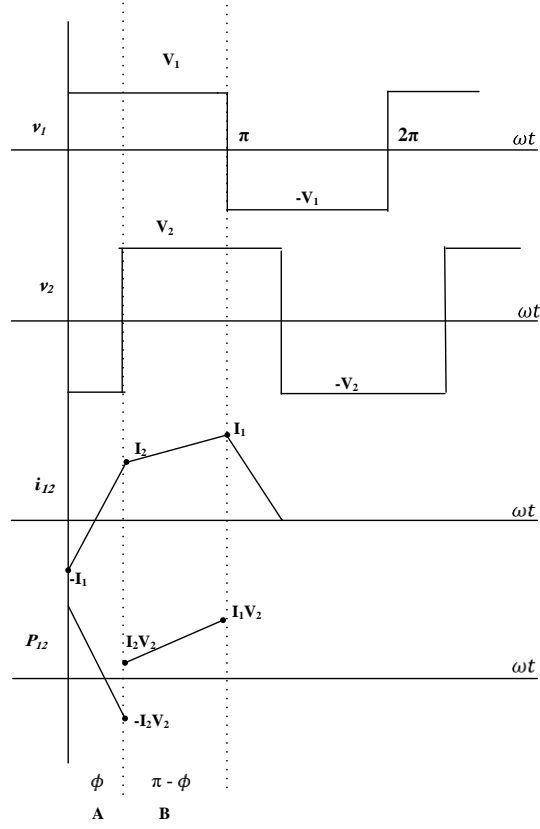
Figure 11. Operating waveforms of DAB.

To find the equation for the power transferred from V_1 to V_2, the inductor current is first

derived during the two operating modes $(0 \leq \theta \leq \phi)$ and $(\phi \leq \theta \leq \pi)$ [23]:

Mode A: $(0 \leq \theta \leq \phi)$

$$L\frac{di_{12}}{dt} = V_1 + V_2 \tag{1}$$

$$\omega L\frac{di_{12}}{d\theta} = V_1 + V_2 \tag{2}$$

$$i_{12}(\theta) = \int_0^\theta \frac{1}{\omega L}(V_1 + V_2)d\theta + (-I_1) \tag{3}$$

$$i_{12}(\theta) = \frac{1}{\omega L} (V_1 + V_2) \theta - I_1 \tag{4}$$

Mode B (t=0 at the start of mode B): $(\phi \le \theta \le \pi)$

$$\frac{di_{12}}{d\theta} = \frac{1}{\omega L} (V_1 - V_2) \tag{5}$$

$$i_{12}(\theta) = \int_0^\theta \frac{1}{\omega L} (V_1 - V_2) \, d\theta + I_2 \tag{6}$$

$$i_{12}(\theta) = \frac{1}{\omega L} (V_1 - V_2) \theta + I_2 \tag{7}$$

Using the boundary condition, equations (4) and (7) can be expressed as

$$i_{12}(\phi) = I_2 = \frac{1}{\omega L} (V_1 + V_2) \phi - I_1 \tag{8}$$

$$i_{12}(\pi) = I_1 = \frac{1}{\omega L} (V_1 - V_2) (\pi - \phi) + I_2 \tag{9}$$

Equivalently

$$I_1 + I_2 = \frac{1}{\omega L} (V_1 - V_2) \phi \tag{10}$$

$$I_1 - I_2 = \frac{1}{\omega L} (V_1 - V_2) (\pi - \phi) \tag{11}$$

The instantaneous power transferred from port 1 to port 2 is given by

$$P_{12} = v_2 \, i_{12} \tag{12}$$

The average power in the interval $[0, \pi]$ becomes

$$\bar{P}_{12} = \frac{1}{\pi} \left[\frac{V_2 (I_1 - I_2)\phi}{2} + \frac{V_2(I_1 + I_2)(\pi - \phi)}{2} \right] \tag{13}$$

By substituting (10) and (11) in (13), the average power is rewritten as

$$\bar{P}_{12} = \frac{V_1 V_2}{\omega L} \phi \left(1 - \frac{|\phi|}{\pi}\right) \qquad (14)$$

From (14) the average current is obtained as

$$\bar{I}_{12} = \frac{V_1}{\omega L} \phi \left(1 - \frac{|\phi|}{\pi}\right) \qquad (15)$$

The absolute term is introduced in order for the power and current equations to be applicable for both positive and negative phase shifts and to obtain a symmetric plot of both equations. The term ϕ represents the direction of power flow. Positive ϕ means that the power is flowing from port 1 to port 2 and negative ϕ means that the current is flowing in the other direction.

The derivation of the average current for TAB or any converter with more than two ports follows the same procedure of DAB. The general circuit for the multiport converter is shown in Figure 12. Each bridge is replaced by a voltage source, and the transformer winding is represented as leakage inductance. The transformer is presented in delta configuration to simplify the analysis. The power flow is controlled by the phase shift with ϕ_1 as a reference. The equations of average power received at port i and average current can be generalized as [24]:

$$\bar{P}_i = \sum_{j=1, j \neq i}^{N} i_{ij} V_i = \sum_{j=1, j \neq i}^{N} V_j V_i Y_{ij} \phi_{ij} \left(1 - \frac{|\phi_{ij}|}{\pi}\right) \qquad (16)$$

$$\bar{I}_i = \sum_{j=1, j \neq i}^{N} i_{ij} = \sum_{j=1, j \neq i}^{N} V_j Y_{ij} \phi_{ij} \left(1 - \frac{|\phi_{ij}|}{\pi}\right) \qquad (17)$$

where N is the total number of ports, V_i and V_j define the ith and jth ports, ϕ_{ij} is the phase shift between the ports i and j, and $Y_{ij} = \frac{1}{\omega L_{ij}}$.

The average current given in (17) is limited to $\phi_{ij} \leq |\pi|$ at which the current reaches its maximum value at $\frac{\pi}{2}$, and it starts decreasing until it reaches π. Beyond π, the current diverges to infinity. In order for the average current equation to accept any value between $-\infty$ and $+\infty$, we have [25]:

$$\bar{I}_i = \sum_{j=1, j \neq i}^{N} V_j Y_{ij} [(-1)^{\tau_{ij}} (\phi_{ij} - \tau_{ij}\pi) \left(1 - \frac{(\phi_{ij} - \tau_{ij}\pi)}{\pi} \right) \tag{18}$$

where

$$\tau_{ij} = floor \left(\frac{\phi_{ij}}{\pi} \right) \tag{19}$$

The value of τ determines the power flow between port i and j as follows:

- $\tau_{ij} = odd\ number$: The average current will be negative. Hence, port j is advanced.

- $\tau_{ij} = even\ number$: The average current will be positive. Hence, port i is advanced.

- $\tau_{ij} = 0$: Equation (18) become (17)
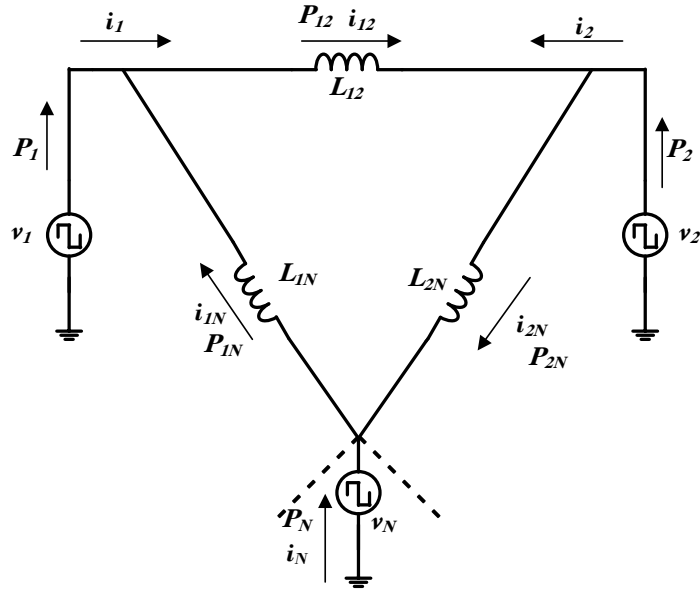
Figure 12. Generalized circuit for multiport converter.

2.2 Multi-Winding Transformer

Various models have been developed for representing the multi-winding transformer and its characteristics [26-29]. One of the simplest representations is to represent the multi-winding transformer as an n-loop circuit consisting of linear elements where each loop is coupled with all other loops electromagnetically. The voltage of the transformer can be represented as

$$V_i = \sum_{i=1}^{n} Z_{ij} I_j \qquad \text{for } 1 \le j \le n \qquad (20)$$

where the mutual impedance is represented by Z_{ij} and the self-impedance of winding i is represented by Z_{ij} for $i = j$. The impedances in (20) can be determined experimentally by applying an open circuit test. However, it should be calculated accurately because the voltage drop in the windings depends on the small variation between Z_{ij} and; Z_{ii}. By

solving the voltage equation and using Cramer's rule, the current can be solved as

$$I_j = \sum_{i=1}^{n} Y_{ij} V_j \quad \text{for } 1 \leq j \leq n \tag{21}$$

where Y_{ij} represent the short circuit transfer admittance and Y_{ij} for $i = j$ is the short-circuit driving point admittances. By applying the short-circuit test, all the admittance parameters can be determined.

In order to analyze and simulate the transformer, it is more convenient to represent an equivalent circuit of the transformer as shown in Figure 13 [22]. In the equivalent circuit for the multi-winding transformer, the number of branches is calculated as $\frac{n(n+1)}{2}$. The admittances represent the magmatic leakage and the winding resistance which provides a damping characteristic during transients. Figure 13 can be further simplified by eliminating the parallel branches if the excitation currents (which are very small compared to the windings current) are neglected. The relation between the admittance coefficient in (21) and the admittance in the equivalent circuit is described as

$$Y_{ij} = -Y_{ji}$$

$$Y_{ii} = \sum_{i \neq j}^{i=1} Y_{ij} \tag{22}$$
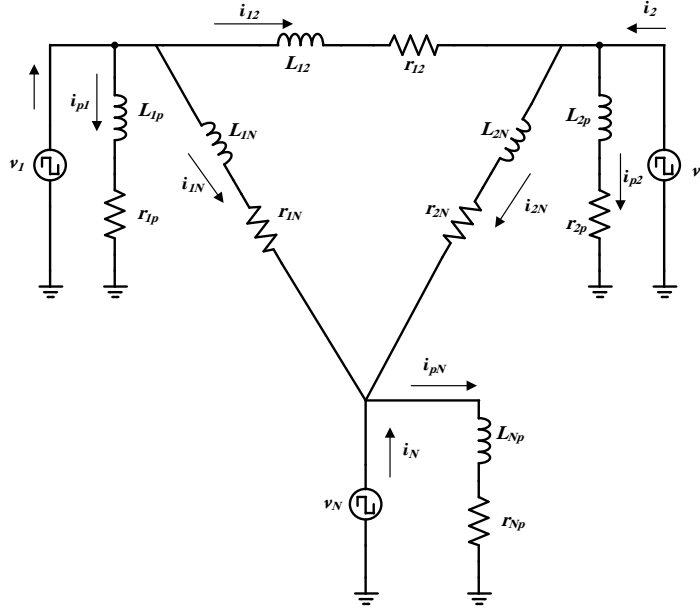
Figure 13. Multi-winding transformer.

2.2.1 Simulation of Multi-Winding Transformer

The simulation of the five-port transformer is done using Matlab/Simulink. The voltage and the power rating of each port are shown in Table 1. Since the UG is selected as a reference port, the base power is same as UG's power rating. The turn ratio is calculated as

$$N_i = \frac{V_i}{V_1} \quad \text{for } i \leq 5 \tag{23}$$

As a result, the voltage at each port is equal to the base voltage of that port. Hence, the per unit voltage for all the ports is equal to 1 and $i_i = P_i$ for $i \leq 5$. Table 2 represents the reactance and the resistance between the ports in per unit. The parameters of the system are per-unitized in order to simplify the analysis. The switching frequency is set to 2 kHz.

Source	Voltage (kV/pu)	Current (A/pu)	Power (MW/pu)
Utility Grid	11/1	-	-
Battery Bank	2/1	250/0.2	0.5/0.2
PV1	1.5/1	333/0.2	0.5/0.2
PV2	1.5/1	333/0.2	0.5/0.2
PV3	1.5/1	333/0.2	0.5/0.2

Table 1. Voltage and power ratings of the five ports.

Resistance and reactance ratings (pu)				
x_{12}	x_{13}	x_{14}	x_{15}	x_{23}
3.3929	3.3929	5.9690	5.5292	3.1416
x_{24}	x_{25}	x_{34}	x_{35}	x_{45}
3.0788	4.1469	3.3929	2.8274	4.3982
r_{12}	r_{13}	r_{14}	r_{15}	r_{23}
0.5830	0.5640	0.3000	0.4200	0.4000
r_{24}	r_{25}	r_{34}	r_{35}	r_{45}
0.3000	0.3500	0.6900	0.6200	0.5500

Table 2. Resistance and reactance ratings for the multi-winding transformer.

Each voltage source is represented by a pulse generator with a variable phase shift. The power transfer is achieved by varying the phase shift between the reference port and the other ports. The simulation is run for two cases to confirm the power transfer between

the ports. In the first case, the BESS phase (ϕ_{12}) will be lagging and in the second case, the same port will be leading to emulate the charging and discharging mode of the BESS. Figure 14-15 show the power transfer from the 4 ports to the battery which is lagging in phase. The contribution of each port to the battery's port is shown in the plots. The average power received by BESS is the summation of the average power of all ports.

(a)　　　　　　　　　　　　　(b)

Figure 14. Current response when ϕ_{12} is delayed by 0.78 rad (45°). (a) UG current (b) BESS current.
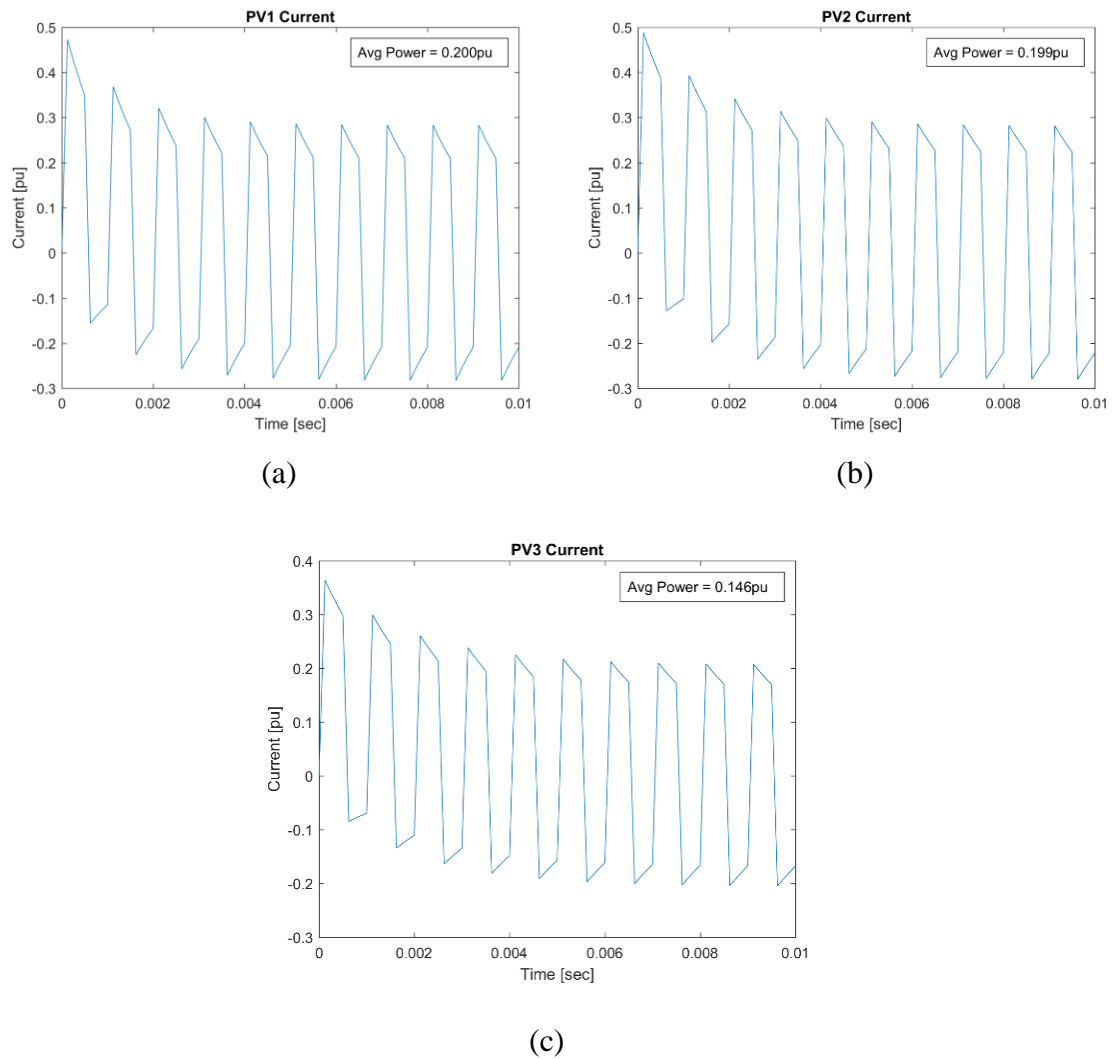
Figure 15. Current response when ϕ_{12} is delayed by 0.78 rad (45°). (a) PV1 current (b) PV2 current (c) PV3 current.

Figures 16-17 represents the power contribution of each port when port 2 is leading. This is done by setting ϕ_{12} to zero and adding a phase shift of 0.78 rad to the other ports. The battery supplies an average power of 0.735 pu to other ports.
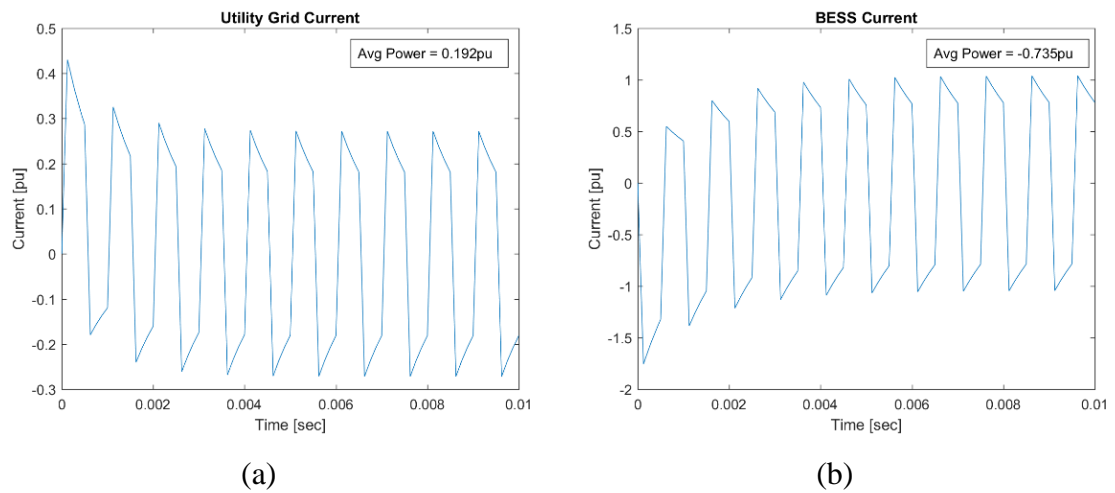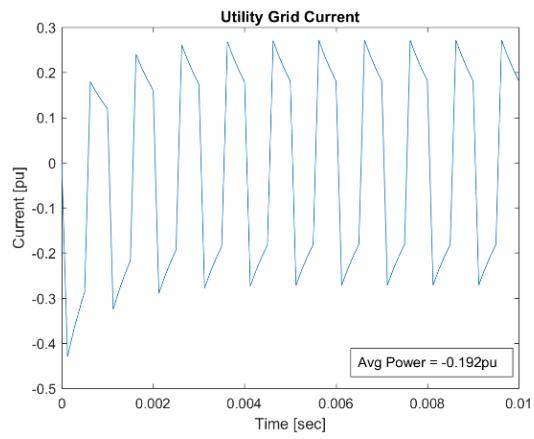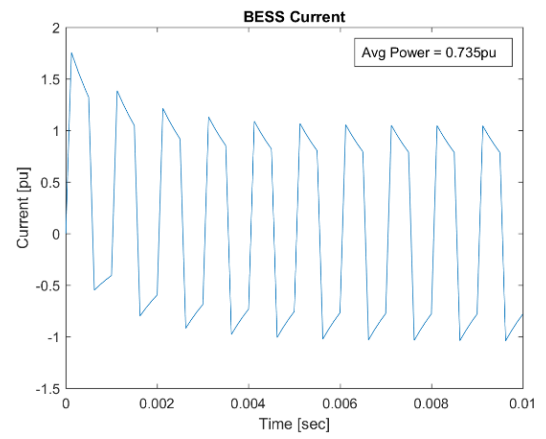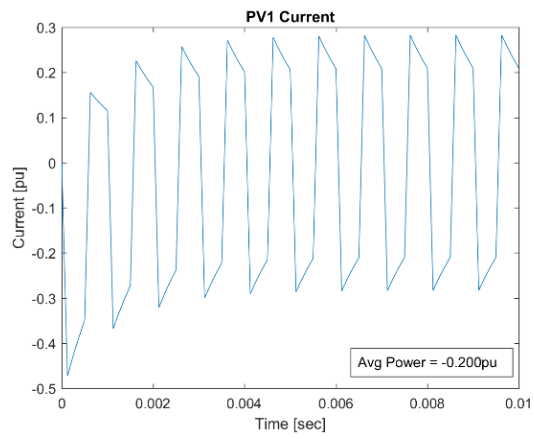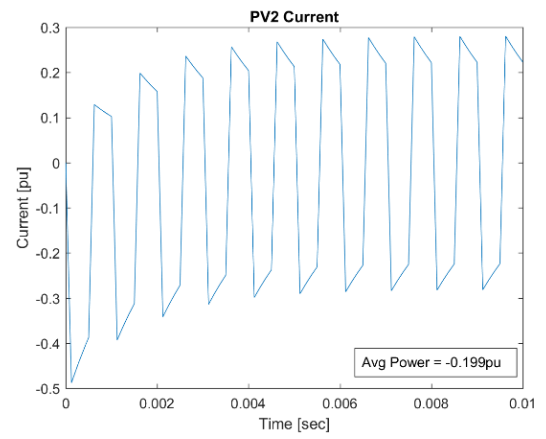
Figure 16. Current response when ϕ_{12} is advanced by 0.78 rad (45°). (a) UG current (b) BESS current (c) PV1 current (d) PV2 current.
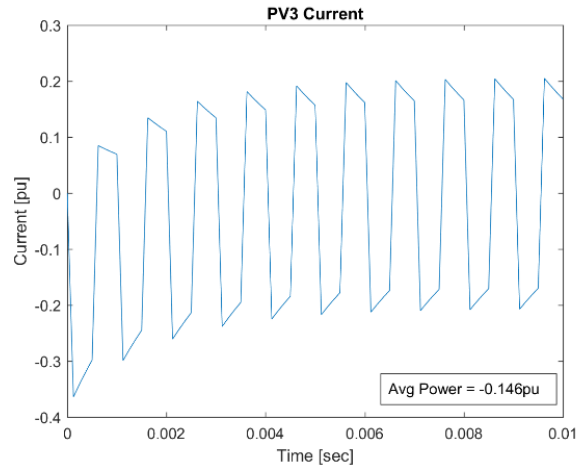
(c)

Figure 17. PV3 current response when ϕ_{12} is advanced by 0.78 rad (45°).

2.3 Multiport Converter Modeling

Modeling multiport converter is useful for simplifying the analysis and for identifying the control strategy suitable for the application. Modeling of the switched converter can be classified into two groups [30]: the detailed switching model and the average value model.

In the detailed switching model, the model includes all the components in the power electronics circuits such as resistor, capacitors, inductors, transistors, etc., and it may also include the parameters of the components such as leakage inductance, series resistance, forward voltage drops, etc. to improve the simulation accuracy [31]. However, due to the switching action in the detailed model, the time domain simulation requires very small time-steps, which can be computationally expensive and very time-consuming. This makes the detailed switching model not suitable for system-level modeling and analysis [31].

The second group, which overcomes the difficulties of the detailed switching model is the Average Value Model (AVM). In the AVM, the switching action of the converter is averaged within a specific time interval. The current and voltage waveforms are all averaged, which helps in simplifying the analysis of the fast switching converters [32]. By averaging the current and voltage waveform, the switching action can be eliminated and replaced by an equivalent average value, which describes the relationship between the circuit variables. AVM allows the use of large time steps in simulation, which makes is it more efficient and reduces the computational time and cost. It can also be linearized around an operating point for small signal analysis of the converter and controller design [32].

There are several approaches that can be used to obtain the AVM, and the most common methods are the circuit averaging [33] and the state-space averaging methods [34]. The circuit averaging approach utilizes the average waveforms of the converter thus allowing the replacement of the switching part of the converter with average circuit components. This approach is more suitable for two or three ports converter since it becomes more time consuming and complex when more ports are added. In the state space averaging method, each operating mode of the converter is described by a state space equation. By using the duty ratio, the weighted average of the state space equations is obtained. This approach is more suitable for the multi-input multi-output system than the circuit averaging method.

In this section, the average current equation from (18) is used to derive the large signal model and its equivalent circuit. The small signal model is obtained by linearizing the large signal model around the operating point. Using the linearized model of the multiport converter, the state space representation is derived. Finally, a detailed model of

multiport converter considering the resistive loss is presented.

2.3.1 Large-Signal Model (LSM)

The large single model of each port is derived from the equivalent circuit shown in Figure 18 which consists of a current source connected to an LC filter and source/sink that represents the type of the port [35] [36]. Each port of the converter is connected to an LC filter as shown in Figure 8. The main objective of adding the filter is to minimize the input/output noise and enhance the system's reliability. The filter can be considered as an input and output filter of each port since the ports are bidirectional. Figure 18a represents the PV port by a dependent source that supplies constant power. In Figure 18b, both BESS and the UG are represented by an open circuit with a constant voltage.

(a)

(b)
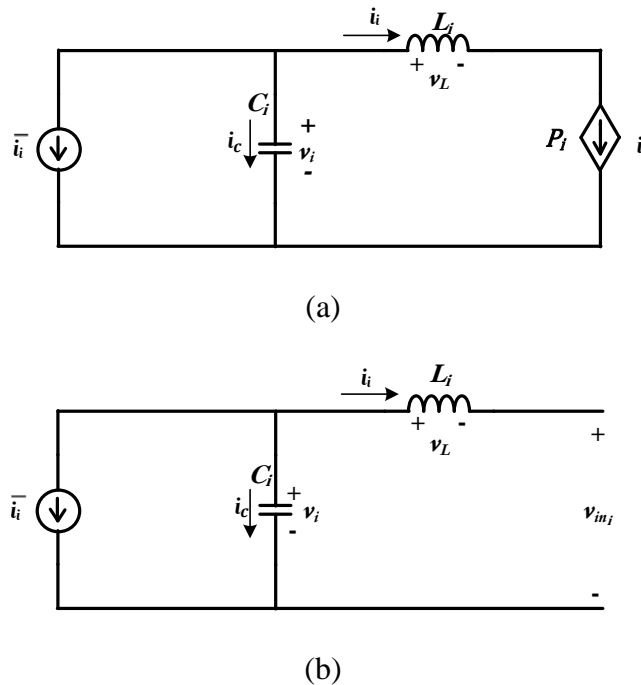
Figure 18. Equivalent circuit of the LC filter connected to the port. (a) PV port (b) UG and BESS ports.

30

The capacitor current i_C is obtained by subtracting the current of the ith port i_i from the average current of the converter $\overline{i_i}$

$$i_C(t) = -i_i(t) - \overline{i_i}(t) \tag{24}$$

where

$$i_C(t) = C_i \frac{dv_i}{dt} \tag{25}$$

The voltage across the capacitor v_i is the same as the port voltage, which can be written as

$$v_i(t) = -\int \left(\frac{\overline{i_i} + i_i}{C_i} \right) dt \tag{26}$$

The PV current can be calculated using

$$i_i = \int \left(\frac{v_i - \frac{P_i}{i_i}}{L_i} \right) dt \tag{27}$$

The UG and BESS current can be expressed as

$$i_i = \int \left(\frac{v_i - v_{in_i}}{L_i} \right) dt \tag{28}$$

where v_{in_i} is the input voltage of the ith port.

2.3.2 Small Signal Model (SSM)

The small signal model is derived by linearizing the equivalent circuits shown in Figure 18 [22, 37]. The voltage across the filter capacitor v_i and the inductor current i_i are selected as states. The operating points of the system are the phase difference between the ports ϕ_{ij}, the steady state capacitor voltage V_j, and inductor current I_i. First, the SSM of the PV port is derived. The same steps are applied for the BESS and UG ports.

PV port

Each operating point can be expressed as a summation of the steady state and the perturbation as follows:

$$\begin{cases} \phi_{ij}(t) = \bar{\phi}_{ij} + \hat{\phi}_{ij}(t) \\ i_i(t) = I_i + \hat{\imath}_i(t) \\ v_j(t) = V_j + \hat{v}_j(t) \end{cases} \tag{29}$$

The voltage across the inductor v_L can be expressed as:

$$v_L(t) = v_i(t) - v_{in_i}(t) \tag{30}$$

$$L\frac{di_i(t)}{dt} = v_i(t) - v_{in_i}(t) \tag{31}$$

The PV voltage can be described as a constant power load and by applying Taylor series expansion [38], the change in v_{PV} can be estimated as

$$V_{in_i} + \hat{v}_{in_i}(t) \cong -\frac{P_i}{I_i} + \frac{P_i}{I_i^2}\hat{\imath}_i(t) \tag{32}$$

Consequently, equation (31) becomes

$$L\frac{d\left(I_i + \overline{\imath_i}(t)\right)}{dt} = \left(V_i(t) + \hat{v}_i(t)\right) + \frac{P_i}{I_i} - \frac{P_i}{I_i^2}\hat{\imath}_i(t) \tag{33}$$

By substituting (24) and (29) in the average current equation (18), the following equation is obtained

$$\sum_{j=1,j\neq i}^{N} Y_{ij}\left(V_j + \hat{v}_j(t)\right)(-1)^{\tau_{ij}}\left(\left(\bar{\phi}_{ij} + \hat{\phi}_{ij}(t)\right) - \tau_{ij}\pi\right)\left(1 - \frac{\left(\left(\bar{\phi}_{ij} + \hat{\phi}_{ij}(t)\right) - \tau_{ij}\pi\right)}{\pi}\right)$$
$$= I_i - \hat{\imath}_i(t) - C\frac{d\left(V_i + \hat{v}_i(t)\right)}{dt} \tag{34}$$

By multiplying terms in equation (34), the following equation is obtained

$$C \frac{d(V_i + \hat{v}_i(t))}{dt} = -I_i - \hat{\iota}_i(t)$$

$$- \sum_{j=1,j\neq i}^{N} (-1)^{\tau_{ij}} Y_{ij} \left[V_j \left(\bar{\phi}_{ij} - \tau_{ij}\pi \right) \left(1 - \frac{\left(\bar{\phi}_{ij} - \tau_{ij}\pi \right)}{\pi} \right) \right]$$

$$- \sum_{j=1,j\neq i}^{N} (-1)^{\tau_{ij}} Y_{ij} \left[\left(\bar{\phi}_{ij} - \tau_{ij}\pi \right) \left(1 - \frac{\left(\bar{\phi}_{ij} - \tau_{ij}\pi \right)}{\pi} \right) \hat{v}_j(t) \right]$$

$$- \sum_{j=1,j\neq i}^{N} (-1)^{\tau_{ij}} Y_{ij} \left[V_j \left(1 - \frac{2\left(\bar{\phi}_{ij} - \tau_{ij}\pi \right)}{\pi} \right) \hat{\phi}_{ij}(t) \right]$$

$$- \sum_{j=1,j\neq i}^{N} (-1)^{\tau_{ij}} Y_{ij} \left[\left(1 - \frac{\left(\bar{\phi}_{ij} + \hat{\phi}_{ij}(t) - \tau_{ij}\pi \right)}{\pi} - \frac{\left(\bar{\phi}_{ij} - \tau_{ij}\pi \right)}{\pi} \right) \hat{v}_j(t)\, \hat{\phi}_{ij}(t) \right]$$

$$+ \sum_{j=1,j\neq i}^{N} (-1)^{\tau_{ij}} Y_{ij} \left[\frac{V_j \hat{\phi}_{ij}(t)^2}{\pi} \right] \tag{35}$$

By assuming that $\hat{v}_j(t) \ll V_j$ and $\hat{\phi}_{ij}(t) \ll \bar{\phi}_{ij}$, the last two terms in (35) are ignored. The

phase shift $\hat{\phi}_{ij}(t)$ can be expressed in terms of $\hat{\phi}_{1j}(t)$ and $\hat{\phi}_{1i}(t)$ to reduce the number of

ϕ terms in the linearized equation

$$\hat{\phi}_{ij}(t) = \hat{\phi}_{1j}(t) - \hat{\phi}_{1i}(t) \tag{36}$$

By placing (36) in (35), the following equation is obtained

$$C \frac{d(V_i + \hat{v}_i(t))}{dt} = -I_i - \bar{\iota}_i(t)$$

$$\sum_{j=1,j\neq i}^{N} K_{ij} V_j + \sum_{j=1,j\neq i}^{N} K_{ij} \hat{v}_j(t) + \sum_{j=2,j\neq i}^{j<i} T_{ij} \hat{\phi}_{1j}(t) - \sum_{j=1,j\neq i,i\neq 1}^{N} T_{ij} \hat{\phi}_{1i}(t) \tag{37}$$

$$+ \sum_{j>1}^{N} T_{ij} \hat{\phi}_{1j}(t)$$

where

$$K_{ij} = (-1)^{\tau_{ij}} Y_{ij} \left(\overline{\phi}_{ij} - \tau_{ij}\pi \right) \left(1 - \frac{\left(\overline{\phi}_{ij} - \tau_{ij}\pi \right)}{\pi} \right) \tag{38}$$

$$T_{ij} = (-1)^{\tau_{ij}} Y_{ij} V_j \left(1 - \frac{2\left(\overline{\phi}_{ij} - \tau_{ij}\pi \right)}{\pi} \right) \tag{39}$$

For the steady-state condition, the DC terms in (33) and (37) are separated, so we have

$$P_i = -V_i I_i \tag{40}$$

$$-I_i - \sum_{j=1,j\neq i}^{N} K_{ij} V_j = 0 \tag{41}$$

Hence, the linear model of the PV port can be obtained from the linear terms in (33) and (37) as follows

$$L\frac{d\hat{i}_i(t)}{dt} = \hat{v}_i(t) - \frac{V_i^2}{P_i}\hat{i}_i(t) \tag{42}$$

$$C\frac{d\hat{v}_i(t)}{dt} = -\hat{i}_i(t) - \sum_{j=1,j\neq i}^{N} K_{ij}\hat{v}_j(t) - \sum_{j=2,j\neq i}^{j<i} T_{ij}\hat{\phi}_{1j}(t)$$

$$+ \sum_{j=1,j\neq i,i\neq 1}^{N} T_{ij}\hat{\phi}_{1i}(t) + \sum_{j>1}^{N} T_{ij}\hat{\phi}_{1j}(t) \tag{43}$$

UG and BESS ports

By following the same procedure as PV port modeling, the steady state and the linearized equations of the UG and BESS ports can be expressed as:

Steady state

$$V_{in1} = V_i \tag{44}$$

34

$$-I_i - \sum_{j=1, j \neq i}^{N} K_{ij} V_j = 0 \tag{45}$$

Linearized equations

$$L \frac{d\hat{\imath}_i(t)}{dt} = \hat{v}_i(t) - \hat{v}_{in1}(t) \tag{46}$$

$$C \frac{d\hat{v}_i(t)}{dt} = -\hat{\imath}_i(t) - \sum_{j=1, j \neq i}^{N} K_{ij} \hat{v}_j(t) - \sum_{j=2, j \neq i}^{j<i} T_{ij} \hat{\phi}_{1j}(t)$$

$$+ \sum_{j=1, j \neq i, i \neq 1}^{N} T_{ij} \hat{\phi}_{1i}(t) + \sum_{j>1}^{N} T_{ij} \hat{\phi}_{1j}(t) \tag{47}$$

2.3.3 State Space Average Model

The state space representation is used to simplify the analysis of the multiport system. The state space average model is obtained by using the linearized equations of the PV, UG, and BESS ports. In the five port converters, the direction of power flow is controlled by varying the angle between the desired port and the reference port (UG), so in this case, there are four phase angles ($\hat{\phi}_{1i}$ for $i \geq 2$) that control the direction of power flow. Moreover, the voltage of UG (v_{in1}) and BESS (v_{in2}) are set by the user, so they are considered as inputs as well. The remaining parameters (the voltage and current of each port) are the states of the system. The state and input vectors for the five-port system are defined as:

$$\begin{cases} \hat{x}(t) = [\, \hat{v}_1(t) \, \dots \, \hat{v}_5(t) \quad \hat{\imath}_1(t) \, \dots \, \hat{\imath}_5(t)] \\ \hat{u}(t) = [\hat{\phi}_{12}(t) \, \dots \, \hat{\phi}_{15}(t) \quad \hat{v}_{in_1}(t) \, \hat{v}_{in_2}(t)] \end{cases} \tag{48}$$

The state space model of five-port DC-DC converter is presented as:

$$\dot{\hat{x}}(t) = A\hat{x}(t) + B\hat{u}(t) \tag{49}$$

$$A = \begin{bmatrix}
0 & -\dfrac{K_{12}}{C_1} & -\dfrac{K_{13}}{C_1} & -\dfrac{K_{14}}{C_1} & -\dfrac{K_{15}}{C_1} & \dfrac{-1}{C_1} & 0 & 0 & 0 & 0 \\[2mm]
-\dfrac{K_{21}}{C_2} & 0 & -\dfrac{K_{23}}{C_2} & -\dfrac{K_{24}}{C_2} & -\dfrac{K_{25}}{C_2} & 0 & -\dfrac{1}{C_2} & 0 & 0 & 0 \\[2mm]
-\dfrac{K_{31}}{C_3} & -\dfrac{K_{32}}{C_3} & 0 & -\dfrac{K_{34}}{C_3} & -\dfrac{K_{35}}{C_3} & 0 & 0 & -\dfrac{1}{C_3} & 0 & 0 \\[2mm]
-\dfrac{K_{41}}{C_4} & -\dfrac{K_{42}}{C_4} & -\dfrac{K_{43}}{C_4} & 0 & -\dfrac{K_{45}}{C_4} & 0 & 0 & 0 & -\dfrac{1}{C_4} & 0 \\[2mm]
-\dfrac{K_{51}}{C_5} & -\dfrac{K_{52}}{C_5} & -\dfrac{K_{53}}{C_5} & -\dfrac{K_{54}}{C_5} & 0 & 0 & 0 & 0 & 0 & -\dfrac{1}{C_5} \\[2mm]
\dfrac{1}{L_1} & 0 & 0 & 0 & 0 & 0 & 0 & 0 & 0 & 0 \\[2mm]
0 & \dfrac{1}{L_2} & 0 & 0 & 0 & 0 & 0 & 0 & 0 & 0 \\[2mm]
0 & 0 & \dfrac{1}{L_3} & 0 & 0 & 0 & 0 & \dfrac{-V_3^2}{P_3\,L_3} & 0 & 0 \\[2mm]
0 & 0 & 0 & \dfrac{1}{L_4} & 0 & 0 & 0 & 0 & \dfrac{-V_4^2}{P_4\,L_4} & 0 \\[2mm]
0 & 0 & 0 & 0 & \dfrac{1}{L_5} & 0 & 0 & 0 & 0 & \dfrac{-V_5^2}{P_5\,L_5}
\end{bmatrix}$$

$$B = \begin{bmatrix}
-\dfrac{T_{12}}{C_1} & -\dfrac{T_{13}}{C_1} & -\dfrac{T_{14}}{C_1} & -\dfrac{T_{15}}{C_1} & 0 & 0 \\[2ex]
\dfrac{\sum_{j=1,j\neq2}^{5} T_{2j}}{C_2} & \dfrac{-2T_{23}}{C_2} & \dfrac{-2T_{24}}{C_2} & \dfrac{-2T_{25}}{C_2} & 0 & 0 \\[2ex]
\dfrac{-T_{32}}{C_3} & \dfrac{\sum_{j=1,j\neq3}^{5} T_{3j}}{C_3} & \dfrac{-T_{34}}{C_3} & \dfrac{-T_{35}}{C_3} & 0 & 0 \\[2ex]
\dfrac{-T_{42}}{C_4} & \dfrac{-T_{43}}{C_4} & \dfrac{\sum_{j=1,j\neq4}^{5} T_{4j}}{C_4} & \dfrac{-T_{45}}{C_4} & 0 & 0 \\[2ex]
\dfrac{-T_{52}}{C_5} & \dfrac{-T_{53}}{C_5} & \dfrac{-T_{54}}{C_5} & \dfrac{\sum_{j=1}^{4} T_{5j}}{C_5} & 0 & 0 \\[2ex]
0 & 0 & 0 & 0 & -\dfrac{1}{L_1} & 0 \\[2ex]
0 & 0 & 0 & 0 & 0 & -\dfrac{1}{L_2} \\[2ex]
0 & 0 & 0 & 0 & 0 & 0 \\[1ex]
0 & 0 & 0 & 0 & 0 & 0 \\[1ex]
0 & 0 & 0 & 0 & 0 & 0
\end{bmatrix}$$

2.3.4 Detailed Model

The LSM and SSM were obtained without considering the winding resistance of the transformer. In high-power applications, the resistance loss can contribute significantly to the efficiency of the system. Figure 19 illustrates the detailed model of the multiport converter for the port connected to UG. The model includes the equivalent circuit of the multi-winding transformer with the winding resistance. The equivalent circuit is obtained by applying Y to delta transformation [39]. The current of any port is expressed as:

$$i_{ij} = \int \left(\frac{v_i - v_j - i_{ij}\, r_{ij}}{L_{ij}} \right) \tag{50}$$

$$i_{pi} = \int \left(\frac{v_i - i_{pi} r_{pi}}{L_{pi}} \right) \tag{51}$$

$$i_i = \sum_{j=1, j \neq i}^{N} i_{ij} + i_{pi} \qquad (52)$$

Another component that is added to the detailed model is the switch model that causes the nonlinear behavior of the converter. Each bridge in the switch is operating with a constant duty cycle of 50%, so a square-wave voltage is generated and transferred to the multi-winding transformer. The current flowing from the multi-winding transformer is demodulated and transferred to the port. By combining (50), (51) and (52) with the LSM equation of any port, the complete detailed model is obtained [24].
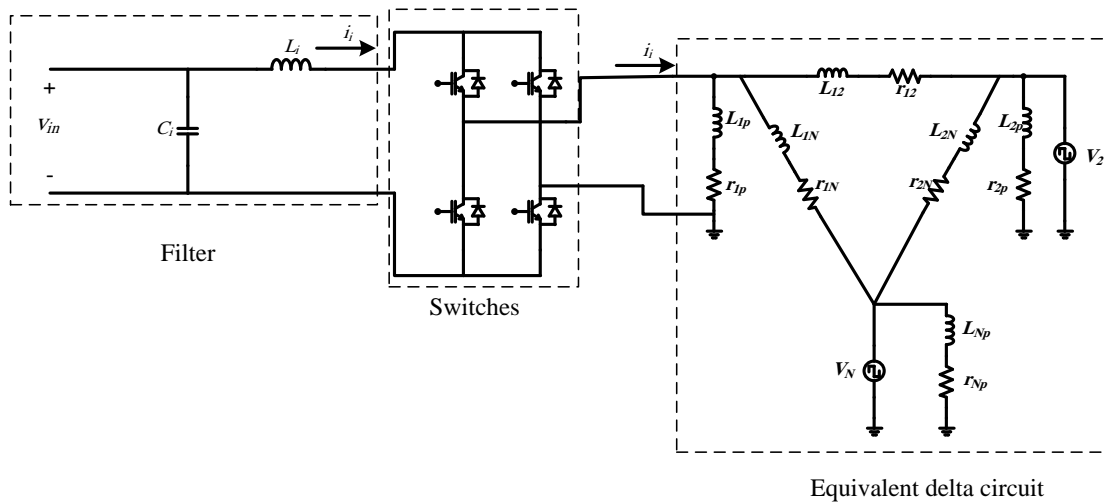

Figure 19. Detailed model of multiport converter.

2.4 Filter Design for the Multiport Converter

Adding a filter to a power converter is essential to attenuate the switching harmonic that appear at the output. The filter also provides protection to the converter and the load from transients in the input voltage which improves the reliability of the system. Several

topologies have been developed for designing filters for DC-DC converters. One of the simplest and most common design is a single stage LC filter. In this section, a mathematical equation is derived for obtaining the minimum L and C based on the required voltage and current ripples. The objective is to have a compacted size of L and C while obtaining an acceptable ripple and without affecting the stability of the system.

In steady state analysis of multiport DC-DC converter, the voltage and current waveforms can be obtained by applying two circuit analysis principles: inductor volt-second balance and capacitor amp-second balance [40]. The inductor volt-second balance states that the average voltage across an ideal inductor must be zero when the current reaches steady state. The capacitor amp-second balance states that the average current through an ideal capacitor must be zero when it reaches steady state. As a result, by obtaining the average inductor current and capacitor voltage through one switching period, the values of L and C can be calculated. The inductor current and capacitor voltage equations can be further simplified by introducing the concept of small ripple approximation. Both equations contain DC components and switching ripples at switching frequency combined by its harmonics. By assuming that the inductor and the capacitor are well designed, the switching ripple magnitude is very small compared to the DC component, so it can be ignored [41].

In the multiport converter under study, applying the small ripple approximation yields zero inductor ripple current since the voltage remains constant throughout the interval regardless of the size of the inductor size [42]. However, physically, although the current ripple of the inductor is small compared to the DC component, it cannot be neglected. In order to better approximate the ripple current, the concept of total flux

approximation is applied [43]. This concept uses the capacitor voltage ripple to accurately estimate the ripple current. Figure 20 shows the voltage and current waveforms of the inductor without DC component [42]. The waveforms are obtained by using the total flux approximation where it is assumed that the ripple voltage of the inductor is caused by the capacitor ripple voltage.
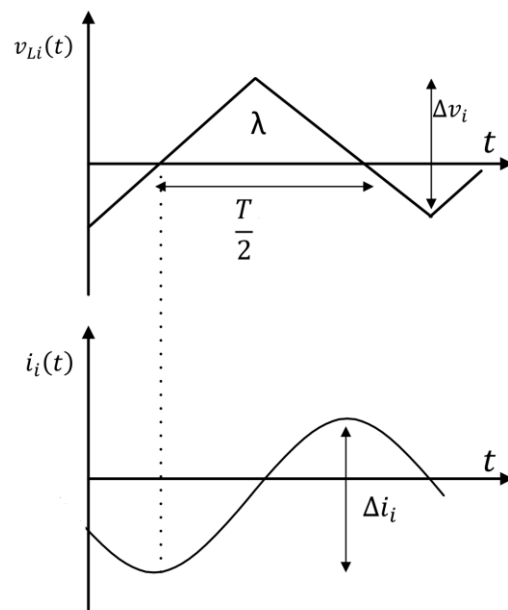

Figure 20. Inductor's voltage and current waveforms.

The total flux λ in the positive part of the inductor voltage is expressed as

$$\lambda = L \, \Delta i \tag{53}$$

The shaded area under the triangle is given by

$$\lambda = \frac{1}{2} \frac{T}{2} \frac{\Delta v_i}{2} \tag{54}$$

Substituting (53) in (54) and solving for L, the relation between the inductor and the

40

ripple current becomes

$$L = \frac{\Delta v_i \, T}{8 \Delta i_i} \tag{55}$$

In the detailed model of the multiport converter, the connection between the LC filter and the converter is illustrated in Figure 19. The switches can be replaced by average ripple current as shown in Figure 21.
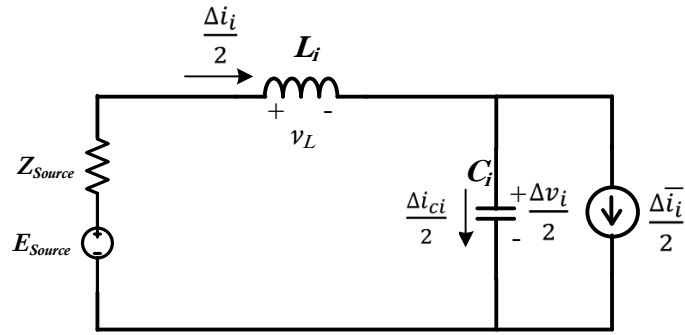

Figure 21. Ripple current circuit.

To simplify the analysis, it is assumed that L and C are large enough to attenuate the ripples to an acceptable value. Under this assumption, the capacitor is considered as a short circuit when analyzing ripple voltage, and the inductor is considered as an open circuit when analyzing the ripple current [44]. As a result, the inductor in Figure 21 acts as a short circuit when analyzing the ripple current so $\Delta i_c = \Delta \overline{i_i}$ and the ripple voltage is given by

$$\Delta v_i = \frac{\Delta \overline{i_i}}{C_i} \tag{56}$$

The average current ripple is expressed as

$$\Delta \overline{i_i} = \overline{I_i} D T_s \tag{57}$$

Using the average current equation in (18) and by substituting in (57), the minimum

capacitance can be calculated

$$C_i = \sum_{j=1, j \neq i}^{N} \frac{V_j D}{2\pi f_s^2 L_{ij} \Delta v_i} \left[(-1)^{\tau_{ij}} (\phi_{ij} - \tau_{ij}\pi) \left(1 - \frac{\phi_{ij} - \tau_{ij}\pi}{\pi} \right) \right] \tag{58}$$

By using the operating points of the system $\phi_{12}, \dots, \phi_{15}$ and by specifying the ripple

voltage and current values, the minimum value of L and C can be obtained. In order for the

filter to operate properly, the following condition must be satisfied.

$$\frac{1}{2\pi \sqrt{L_i C_i}} \ll f_s \tag{59}$$

Table 3 shows the selected values for the LC filter for the five-port converter under study.

The ripple current is set to 10% of $i_1, \dots, i_5$ and ripple voltage to 5% of $v_1 \dots v_5$.

Port type	C (mF/pu)	L (mH/pu)
UG	0.6/36.3e-3	0.9/0.015e-3
BESS	0.25/1e-3	0.62/0.6e-3
PV1	0.12/0.8e-3	1.2/1.5e-3
PV2	0.45/1e-3	0.2/0.7e-3
PV3	0.17/0.9e-3	0.53/0.9e-3

Table 3. Selected inductor and capacitor values.

2.5 Summary

In this chapter, the operation and characteristics of multiport converter is discussed. The operating waveforms of a DAB converter is presented and used to derive the generalized form of the average current and power equations. The equivalent circuit of the multi-winding transformer is illustrated, and a simulation is carried out to demonstrate the power transfer between the ports by varying the phase angles. In addition, the large-signal model for each port is obtained and the equivalent circuit for each port is presented. The linearization of the large-signal model is done in order to derive the small-signal model which is used to build the state space representation of the five-port converter. Moreover, the detailed model which includes the winding resistance of the multiwinding transformer and the switching model is presented. Finally, an LC filter is designed, and the equations for calculating the minimum inductor and capacitors values are derived.

CHAPTER 3: MULTIPORT CONVERTER CONTROLLER

To ensure a stable operation of the converter is maintained regardless of the operating conditions and to guarantee fast and stable recovery in transient event, a closed-loop control system is required. A non-linear system such as the multiport converter system can be either controlled using a non-linear controller such as sliding mode controller [45] or using a linear controller such as PID controller [46], and state feedback control [47]. Linear controllers are easier to design and provide better performance if the linear model is obtained accurately.

Before selecting the linear controller, the non-linear model of the multiport converter must be linearized around an operating point. PI controller is commonly used in various DC-DC converters such as buck, boost, and buck-boost converter due to its simple design and implementation [48]. However, it has low robustness especially when the system encounters disturbances which compromises the transient response of the system. Moreover, PI and PID controller is typically used in single-input single-output (SISO) systems. State feedback control overcomes some of the disadvantages of PID control such as providing a better dynamic response under disturbance, and it is applicable for multi-input multi-output (MIMO) system such as the multiport converter under study. The transient response (specifically the overshoot) is an important factor that must be taken into consideration when designing a controller to provide better protection for the physical system. To enhance the overshoot response of the system, a non-overshooting controller is introduced which is capable of eliminating the overshoot and provide a smooth response [49].

This chapter will study the design and simulation of state feedback control using

the linearized model obtained in Chapter 3. The control system is then applied to the five-port system on Matlab/Simulink. In addition, non-overshooting control is introduced and applied to the closed-loop system, and the result is discussed. Finally, two fault scenarios are simulated to evaluate the system response under fault conditions using optimal controller and non-overshooting controller.

3.1 State Feedback Control

In the state feedback control, the objective is to find the feedback gain from a linear combination of the state variables. There are two approaches for designing state feedback control depending on the available states [50]. The first approach assumes that all the states are available. In this case, the control law can be obtained and directly applied to the system. This approach may not be valid for most real-life applications where there is no accessibility for all the states of the system. In such systems, the second approach is more valid which includes designing an observer to estimate all the states using parameters from the output. In the multiport system under study, all the states can be measured which can simplify the process of obtaining the control law.

The general state space representation of the five-port system was presented in Section 2.3.3. This representation can be re-arranged according to the design requirement. Since the UG input voltage (v_{in1}) and the BESS input voltage (v_{in2}) are not controlled by the designer, they are considered as known constant inputs to the system. The selected trackable references are $i_2, i_3, i_4 \ and \ i_5$ which are BESS, PV1, PV2, and PV3 current, respectively. The modified state space representation is given by

$$\dot{\hat{x}}(t) = A\hat{x}(t) + B\hat{u}(t) + E\hat{w} \qquad (60)$$

$$y(x) = C\hat{x}(t)$$

where $\hat{x}(t) = [\ \hat{v}_1(t) \ ... \ \hat{v}_5(t) \quad \hat{i}_2(t) \ ... \ \hat{i}_5(t)]^T$, $\hat{u}(t) = [\hat{\phi}_{12}(t) \ ... \ \hat{\phi}_{15}(t)]$, and $\hat{w} = [v_{in1} \quad v_{in2}]^T$.

$$A = \begin{bmatrix}
0 & -\dfrac{K_{12}}{C_1} & -\dfrac{K_{13}}{C_1} & -\dfrac{K_{14}}{C_1} & -\dfrac{K_{15}}{C_1} & \dfrac{1}{C_1} & \dfrac{1}{C_1} & \dfrac{1}{C_1} & \dfrac{1}{C_1} \\
-\dfrac{K_{21}}{C_2} & 0 & -\dfrac{K_{23}}{C_2} & -\dfrac{K_{24}}{C_2} & -\dfrac{K_{25}}{C_2} & -\dfrac{1}{C_2} & 0 & 0 & 0 \\
-\dfrac{K_{31}}{C_3} & -\dfrac{K_{32}}{C_3} & 0 & -\dfrac{K_{34}}{C_3} & -\dfrac{K_{35}}{C_3} & 0 & -\dfrac{1}{C_3} & 0 & 0 \\
-\dfrac{K_{41}}{C_4} & -\dfrac{K_{42}}{C_4} & -\dfrac{K_{43}}{C_4} & 0 & -\dfrac{K_{45}}{C_4} & 0 & 0 & -\dfrac{1}{C_4} & 0 \\
-\dfrac{K_{51}}{C_5} & -\dfrac{K_{52}}{C_5} & -\dfrac{K_{53}}{C_5} & -\dfrac{K_{54}}{C_5} & 0 & 0 & 0 & 0 & -\dfrac{1}{C_5} \\
0 & \dfrac{1}{L_2} & 0 & 0 & 0 & 0 & 0 & 0 & 0 \\
0 & 0 & \dfrac{1}{L_3} & 0 & 0 & 0 & \dfrac{-V_3^2}{P_3 L_3} & 0 & 0 \\
0 & 0 & 0 & \dfrac{1}{L_4} & 0 & 0 & 0 & \dfrac{-V_4^2}{P_4 L_4} & 0 \\
0 & 0 & 0 & 0 & \dfrac{1}{L_5} & 0 & 0 & 0 & \dfrac{-V_5^2}{P_5 L_5}
\end{bmatrix}$$

$$B = \begin{bmatrix}
-\dfrac{T_{12}}{C_1} & -\dfrac{T_{13}}{C_1} & -\dfrac{T_{14}}{C_1} & -\dfrac{T_{15}}{C_1} \\
\dfrac{\sum_{j=1,j\neq2}^{5} T_{2j}}{C_2} & \dfrac{-2T_{23}}{C_2} & \dfrac{-2T_{24}}{C_2} & \dfrac{-2T_{25}}{C_2} \\
\dfrac{-T_{32}}{C_3} & \dfrac{\sum_{j=1,j\neq3}^{5} T_{3j}}{C_3} & \dfrac{-T_{34}}{C_3} & \dfrac{-T_{35}}{C_3} \\
\dfrac{-T_{42}}{C_4} & \dfrac{-T_{43}}{C_4} & \dfrac{\sum_{j=1,j\neq4}^{5} T_{4j}}{C_4} & \dfrac{-T_{45}}{C_4} \\
\dfrac{-T_{52}}{C_5} & \dfrac{-T_{53}}{C_5} & \dfrac{-T_{54}}{C_5} & \dfrac{\sum_{j=1}^{4} T_{5j}}{C_5} \\
0 & 0 & 0 & 0 \\
0 & 0 & 0 & 0 \\
0 & 0 & 0 & 0 \\
0 & 0 & 0 & 0
\end{bmatrix}$$

$$E = \begin{bmatrix} 0 & 0 & 0 & 0 & 0 & 0 & -\dfrac{1}{L_2} & 0 & 0 \end{bmatrix}^T$$

$$C = \begin{bmatrix} 0 & 0 & 0 & 0 & 0 & 1 & 0 & 0 & 0 \\ 0 & 0 & 0 & 0 & 0 & 0 & 1 & 0 & 0 \\ 0 & 0 & 0 & 0 & 0 & 0 & 0 & 1 & 0 \\ 0 & 0 & 0 & 0 & 0 & 0 & 0 & 0 & 1 \end{bmatrix}$$

In order to design a robust state feedback control with adequate disturbance rejection capability, there are two problems that must be solved: the regulator problem and tracking problem. The regulator problem arises when a disturbance such as sudden change in the load current or the BESS voltage causes the system to deviate from its initial condition. It requires a state feedback gain to set the deviation to zero and force the system to die out at the desired value. The tracking problem is related to designing state feedback at which the output $y(t)$ tracks the reference input y_d as t approaches infinity. In addition to the state feedback gain K, feedforward integrator gain K_a is added to reduce the steady state error. Figure 22 illustrates the state feedback system for the five-port converter. The control system consists of the state feedback model and the non-linear detailed model of the converter [24].
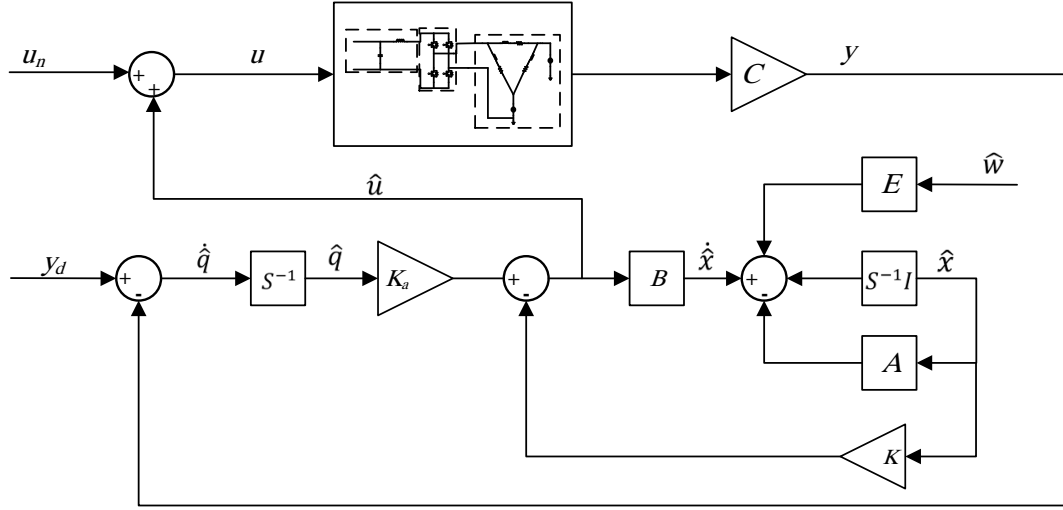
Figure 22. The control system for five-port converter.

The closed-loop system with the integral state feedback controller is described by

$$\begin{bmatrix} \dot{\hat{x}}(t) \\ \dot{\hat{q}}(t) \end{bmatrix} = \begin{bmatrix} A & 0 \\ -C & 0 \end{bmatrix} \begin{bmatrix} \hat{x}(t) \\ \hat{q}(t) \end{bmatrix} + \begin{bmatrix} B \\ 0 \end{bmatrix} \hat{u}(t) + \begin{bmatrix} E \\ 0 \end{bmatrix} \hat{w} + y_d \qquad (61)$$

$$\hat{y}(t) = \begin{bmatrix} C & 0 \end{bmatrix} \begin{bmatrix} \hat{x}(t) \\ \hat{q}(t) \end{bmatrix} \qquad (62)$$

where

$$\hat{u}(t) = \begin{bmatrix} -K & K_a \end{bmatrix} \begin{bmatrix} \hat{x}(t) \\ \hat{q}(t) \end{bmatrix} \qquad (63)$$

The error signal dynamics is given as

$$\dot{\hat{q}}(t) = y_d - y(t) \qquad (64)$$

Since all the states are available in the multiport system, we can proceed to the next step which involves checking the controllability of the system. In order to design a state feedback control capable of adjusting system parameter such as settling time, overshoot and steady state error, the system must be controllable. A system is considered to be

48

controllable if there exists an input which transfers the states of the system from the initial state to the desired state in a finite time interval [50]. Mathematically, the system is said to be controllable if the following condition is satisfied

$$rank\ [B\quad AB\quad ...\ A^{n-1}B] = n$$

In order to stabilize the system and obtain the required response, the feedback gain K must be selected. The common technique for assigning the gain matrix K is by using the pole placement approach where a set of poles are selected that will correspond to the dynamic response of the system. A more effective method for assigning the gain matrix is to optimally assign it using Liner Quadratic Regulator (LQR) [51]. In LQR, the goal is to minimize the quadratic cost function J given by

$$J = \int_0^\infty (x^T Q x + u^T R u) dt \tag{65}$$

where the weighting matrices Q and R impose a tradeoff between the variation of the states from the origin and the control effort respectively. The solution to this optimal system can be found from

$$K = R^{-1} B^T P \tag{66}$$

Where P is a unique positive definite solution to the Riccati equation given by

$$PA + A^T P - PBR^{-1}B^T P + Q = 0 \tag{67}$$

The solution of this equation can be simply obtained on Matlab using lqr command. The gain matrix obtained here represent both the feedback gain with K^{nxn} and K_a^{mxn} . For the

five-port converter under study, the weighting matrices are selected as $Q = diag(1,1,1,1,1,1,1000,1000,10,200,500,200,2000)$ and $R = I_{4\times4}$.

3.1.1 Simulation Result

The simulation is run for three modes to illustrate the response of the system under different conditions. The selected trackable inputs are i_2, i_3, i_4 and i_5. The UG desired current value represents the summation of $i_2, ..., i_5$. Figures 23-24 show the current of all the ports for the different modes. The figures show the output starting at 20 sec because it is assumed that the system is run under steady state condition before the variation in the desired output is applied. In the first case, the desired output is set to $y_d = [0.2019 - 0.0308 - 0.1298 - 0.2009]$ where the three PV units are supplying the BESS and the UG at different power rates. This case represents the converter operation during the daytime. At 30 sec the new desired output is set to $y_{d2} = [0.1019 - 0.108 - 0.2 \ 0]$. In this case, it is assumed that PV3 is not able to supply any current to the system so i_5 is set to zero. At 50 sec the system is operating during night time where only BESS is supplying the UG, and all the PVs are off. The desired value in this case is set to $y_{d3} = [-0.2 \ 0 \ 0 \ 0]$. The steady state error in UG current is due to numerical error caused by the solver used in Simulink. Figures 25-26 show the voltage of each port under the variation of the desired output. The voltage remains constant at 1 pu throughout the simulation. At 20 sec and 40 sec the desired output is changed, the voltage oscillates for around 5 sec before is settles to 1 pu. The voltage ripple can be enhanced by selecting the larger capacitor, but the response of the system will be slower.
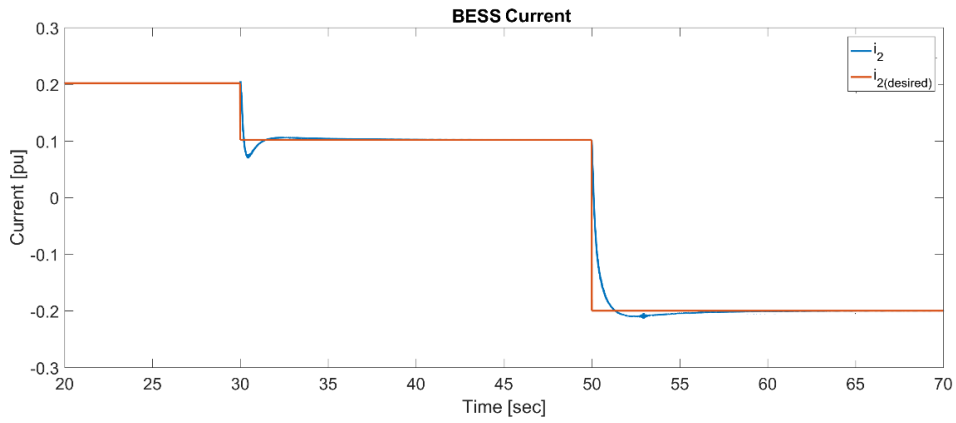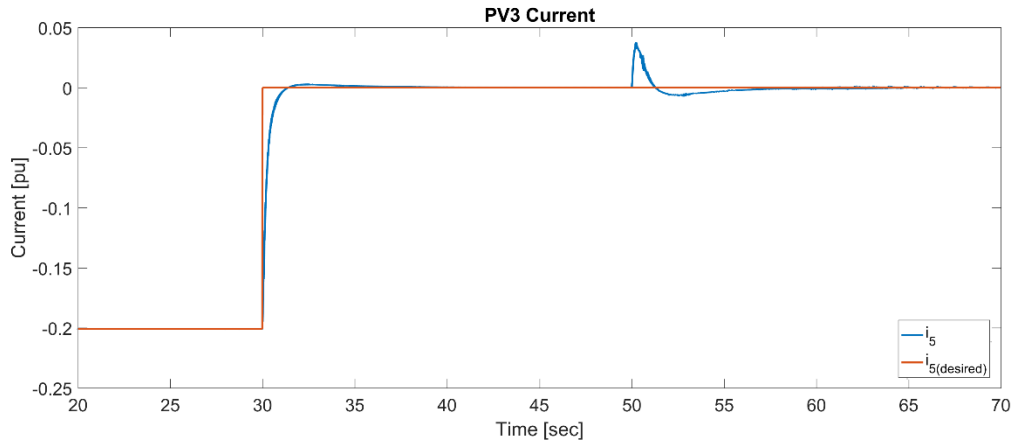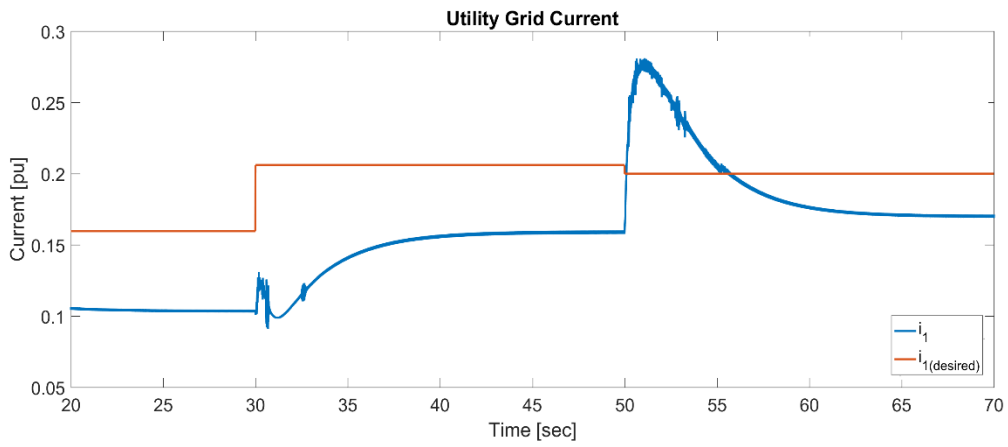
(a)
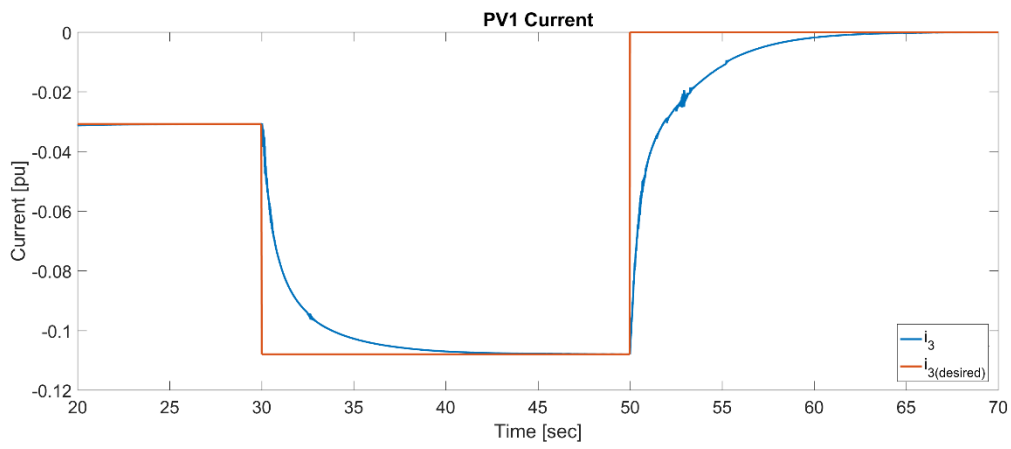
(b)
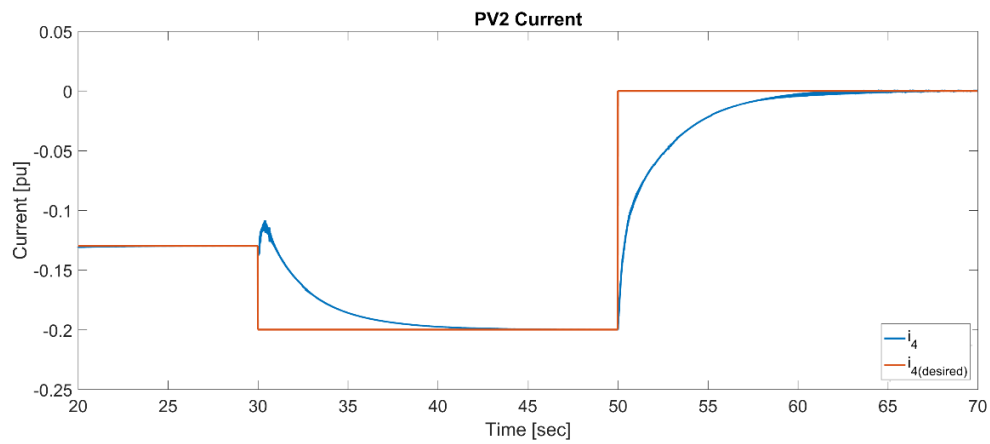
(c)

Figure 23. Current response under different operating conditions. (a) BESS current (b)
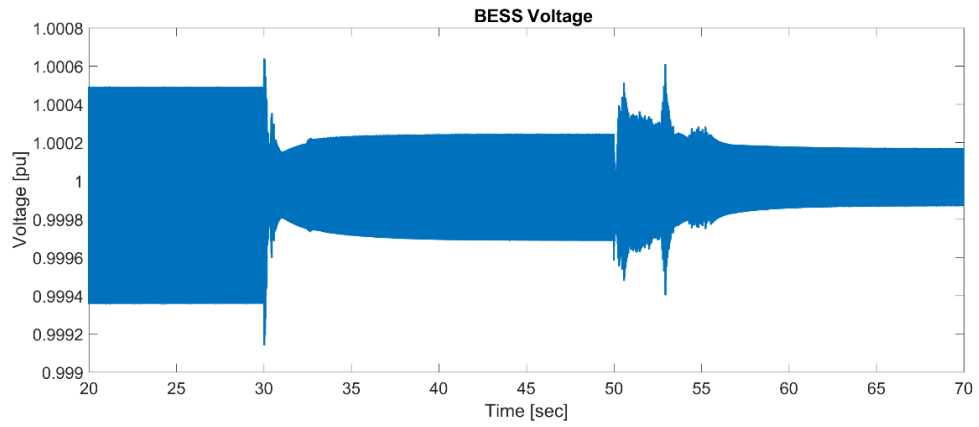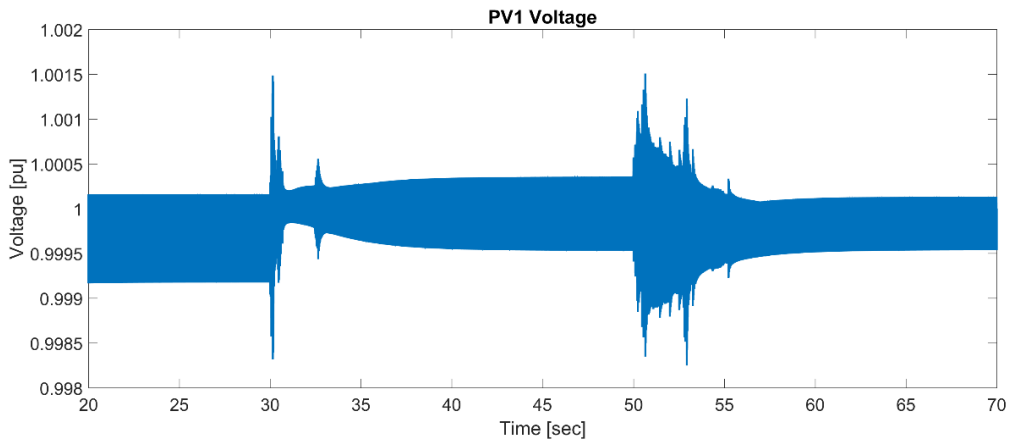
PV1 current (c) PV2 current.
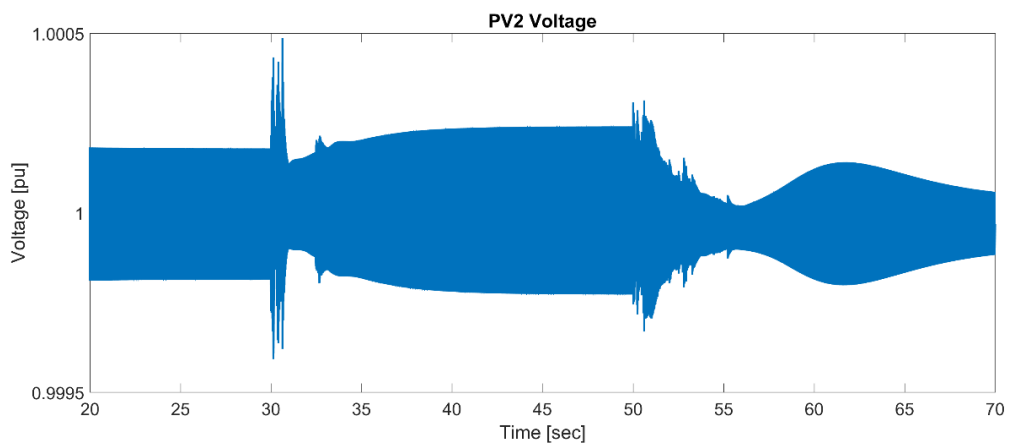
(a)

(b)

Figure 24. Current response under different operating conditions. (a) PV3 port current (b) UG port current.
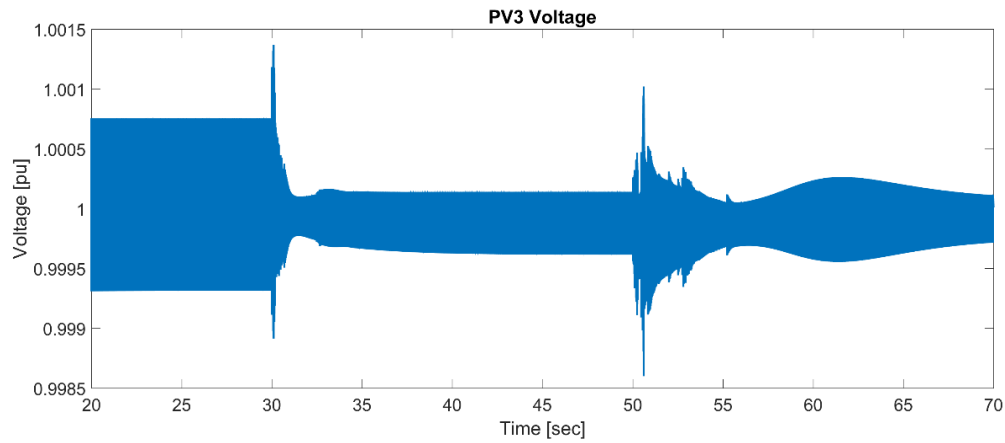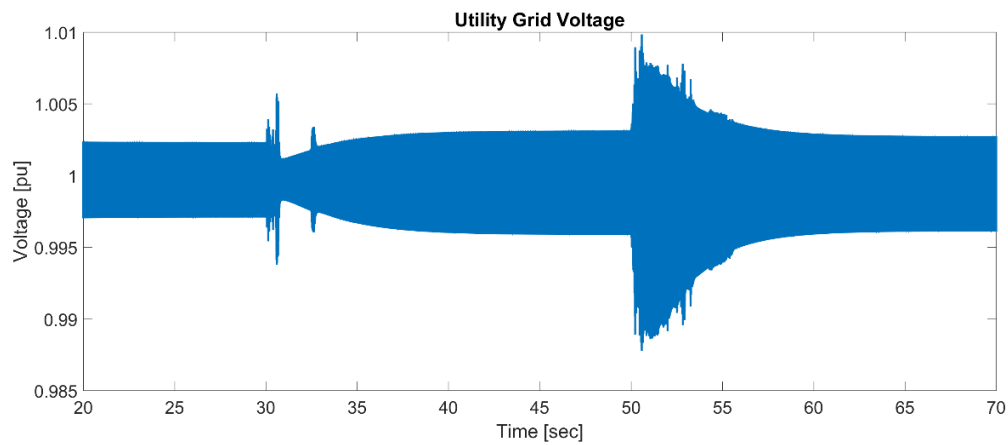
(a)

(b)

(c)

Figure 25. Voltage response under different operating conditions. (a) BESS port voltage

(b) PV1 port voltage (c) PV2 voltage.

(a)

(b)

Figure 26. Voltage response under different operating conditions. (a) PV3 port voltage
(b) UG port voltage.

3.2 Non-Overshooting Controller

In the previous section, an optimal controller was designed for the state feedback system. It is noted that during the transient response, there is a high overshoot. The reason for that is there are modes which are appearing in the output that are contributing to the overshoot of the system. The objective of the non-overshooting controller is to have only

selected modes to appear in each output by using eigen-structure assignment for MIMO system [52]. The method includes combining the closed-loop eigenvalue and eigenvector to obtain the state feedback gain. MIMO system provides the flexibility of obtaining multiple sets of eigenvectors without varying the closed-loop eigenvalues. The non-overshoot step response is then achieved by distributing the stable modes evenly where each component of the tracking error has one exponential non-overshooting mode [49]. The system in (61) is used to design a control law such that the output tracks the desired output accurately without overshoot.

The number of modes that appear in each element of the output signal $y(t)$ depends on the invariant zeros $Z = \{z_1, \dots, z_{\hat{n}-lp}\}$ of the system where $\hat{n} = n + p$. For a system with $\hat{n} - lp$ invariant zeros, the selection of the closed-loop eigenvalues $L = \{\lambda_1, \dots, \lambda_{\hat{n}}\}$ is done based on the number of the invariant zeros of the system where $\lambda_i = z_i$ for i $\in \{1, \dots, \hat{n} - lp\}$ and the remaining eigenvalues λ_i can be selected as any real asymptotical stable modes i $\in \{1, \dots, \hat{n} - lp\}$. Let $S = \{s_1, \dots, s_{\hat{n}}\}$, $s_i \in R^p$, such that

$$s_i = \begin{cases} 0 \ for \ i \in \{1, \dots, \hat{n} - lp\} \\ e_1 \ for \ i \in \{\hat{n} - lp + 1, \dots, \hat{n} - lp + l\} \\ \qquad \qquad . \\ \qquad \qquad . \\ \qquad \qquad . \\ e_p \ for \ i \in \{\hat{n} - l + 1 \dots, \hat{n}\} \end{cases} \qquad (68)$$

where $e_i, i = 1, \dots, p$ are basis vectors in R^p. In order to calculate the gain matrix, the following matrix equation

$$\begin{bmatrix} A - \lambda I & B \\ C & D \end{bmatrix} \begin{bmatrix} v_i \\ w_i \end{bmatrix} = \begin{bmatrix} 0 \\ s_i \end{bmatrix} \qquad (69)$$

is assumed to have a solution sets $V = \{v_1, \ldots, v_{\hat{n}}\} \subset C^{\hat{n}}$ and $W = \{w_1, \ldots, w_{\hat{n}}\}$ for $i \in \{1, \ldots, \hat{n}\}$. Giving that V is linearly independent, a unique feedback gain K_c is obtained such the for $i \in \{1, \ldots, \hat{n}\}$,

$$(A + BK_c)v_i = \lambda_i v_i \tag{70}$$

$$(C + DK_c)v_i = s_i \tag{71}$$

By using Moore algorithm in [52], the feedback gain matrix is calculated as

$$K_c = WV^{-1} \tag{72}$$

For i $\in \{1, \ldots, n - lp\}$, the solution of the matrix $\begin{bmatrix} v_i \\ w_i \end{bmatrix}$ is the null space of the

Rosenbrock matrix $P_{\Sigma.} \begin{bmatrix} A - \lambda I & B \\ C & D \end{bmatrix}$ where $\lambda_i = z_i$. After obtaining the gain matrix, the

following steps are done to verify that the gain matrix obtained in (72) is capable of eliminating the overshoot and provide a good transient response. For $k \in \{1, \ldots, p\}$, let $v_{k1}, v_{k2}, \ldots, v_{kp}$ be the eigenvectors in V associated with the canonical basis vector e_p and let $\lambda_{k1}, \lambda_{k2}, \ldots, \lambda_{kp}$ be the corresponding eigenvalues ordered such that $\lambda_{k1} < \lambda_{k2} < \ldots, \lambda_{kp}$.

The system in (61) can be re-written as

$$\dot{x}_c(t) = A_a x_c(t) + B_a \hat{u}(t) + D_a \tag{73}$$

$$\hat{y}(t) = [C \quad 0]x_c(t) = C_a x_c(t) \tag{74}$$

where $x_c(t) = [\hat{x}(t) \quad \hat{q}(t)]^T$, $D_a = E_a \hat{w} + y_d$, $A_a = \begin{bmatrix} A & 0 \\ -C & 0 \end{bmatrix}$, $B_a = \begin{bmatrix} B \\ 0 \end{bmatrix}$, $E_a = \begin{bmatrix} E \\ 0 \end{bmatrix}$,
$\hat{u}(t) = [-K \ K_a] x_c(t) = K_c x_c(t)$

The closed-loop system is given by

$$x_c(t) = e^{\hat{A}t}x_{a0} + \int_0^t e^{\hat{A}(t-\tau)}D_a d\tau = e^{\hat{A}t}x_{a0} + e^{\hat{A}t}\hat{A}^{-1}D_a - \hat{A}^{-1}D_a \tag{75}$$

The state transition matrix can be written as $e^{\hat{A}t} = Ve^{\Lambda t}V^{-1}$ where Λ is a diagonal matrix with the eigenvalues $\lambda_1, \dots, \lambda_{\hat{n}}$ on the diagonal. Therefore,

$$x_c(t) = Ve^{\Lambda t}V^{-1}x_{a0} + Ve^{\Lambda t}V^{-1}\hat{A}^{-1}D_a - \hat{A}^{-1}D_a$$

Now let $\alpha = [\alpha_1 \dots \alpha_{n-lp}, \ \alpha_{1,1} \dots \alpha_{1,l} \quad \alpha_{1,p} \dots \alpha_{p,l}]^T = V^{-1}x_{a0}$ and $\beta = V^{-1}\hat{A}^{-1}D_a$.

Given that $C_a v_i = s_i$ for $i = 1, \dots, \hat{n}$, the output $y(t)$ can be described as

$$y(t) = \sum_{i=1}^{\hat{n}} C_a v_i \alpha_i e^{\lambda_i t} + \sum_{i=1}^{\hat{n}} C_a v_i \beta_i e^{\lambda_i t} - \sum_{i=1}^{\hat{n}} C_a v_i \beta_i$$

$$= \sum_{i=\hat{n}-lp+1}^{\hat{n}} e_{i-(\hat{n}-lp)}\gamma_i e^{\lambda_i t} + D \tag{76}$$

where $\gamma_i = \alpha_i + \beta_i$ and $D = -\sum_{i=1}^{\hat{n}} C_a v_i \beta_i$.

In the five-port system under study, the total number of invariant zeros is one which means that $\hat{n} - lp = 1$, where $\hat{n} = 13$, $l = 3$ and $p = 4$. The remaining 12 closed-loop poles are selected within this range [-10,-100]. Therefore, in each output, three different eigenvalues are appeared.

Let $\lambda_1 < \lambda_2 < \lambda_3$ and define

$$f(t) = \gamma_1 e^{\lambda_1 t} + \gamma_2 e^{\lambda_2 t} + \gamma_3 e^{\lambda_3 t}$$

In order for the system to not have an overshoot, there should be no sign change in the function $f(t)$ and that is achieved in the following conditions:

    I. $\gamma_1.\gamma_2 > 0, \gamma_1.\gamma_3 < 0, and \ |\gamma_1 + \gamma_2| > |\gamma_3|$;

    II. $\gamma_2.\gamma_3 > 0, \gamma_1.\gamma_2 < 0, and \ |\gamma_1| > |\gamma_2 + \gamma_3|$;

III. (a) $\gamma_1 \cdot \gamma_3 > 0, \gamma_1 \cdot \gamma_2 < 0, and\ |\gamma_2| > |\gamma_1 + \gamma_3|$;

IV. (b) $\gamma_1 \cdot \gamma_3 > 0, \gamma_1 \cdot \gamma_2 < 0, |\gamma_2| > |\gamma_1 + \gamma_3|\ and\ t^* > 0\ and\ |g_c(t^*)| \geq$

$|\gamma_1 + \gamma_2 + \gamma_3|$

where

$$t^* = \frac{1}{\lambda_3 - \lambda_1} \ln \left(\frac{\gamma_1(\lambda_2 - \lambda_1)}{\gamma_3(\lambda_3 - \lambda_2)} \right)$$

$$g_c(t) = \gamma_1 \left(1 - e^{(\lambda_1 - \lambda_2)t} \right) + \gamma_3 \left(1 - e^{(\lambda_3 - \lambda_2)t} \right)$$

3.2.1 Simulation Result

The system is simulated using the non-overshooting controller under the same three operating modes used in the optimal controller and the output of both controllers are compared as shown in Figures 27-30 . It is noted that for $i_2, \dots, i_5$, there is a big reduction in overshoot when applying the non-overshoot controller. When using the optimal controller, the overshoot reaches to approximately 30% in i_2 and 15% in i_4 and the settling time is approximately 20 sec for $i_1, i_3,$ and i_4. However, when using the non-overshooting controller, the maximum overshoot is at approximately 1% and the settling time is around 5 sec or less. In addition, the UG current steady state error has reduced from 0.03 pu to 0.01 pu. The small overshoot that appears in some outputs such as i_2 and i_5 when using a non-overshooting controller is due to the fact that the controller is applied to a nonlinear model. The overshoot could be further reduced by selecting a different set of eigenvalues. The voltage response has also significantly improved compared to the optimal controller in terms of overshoot and settling time.
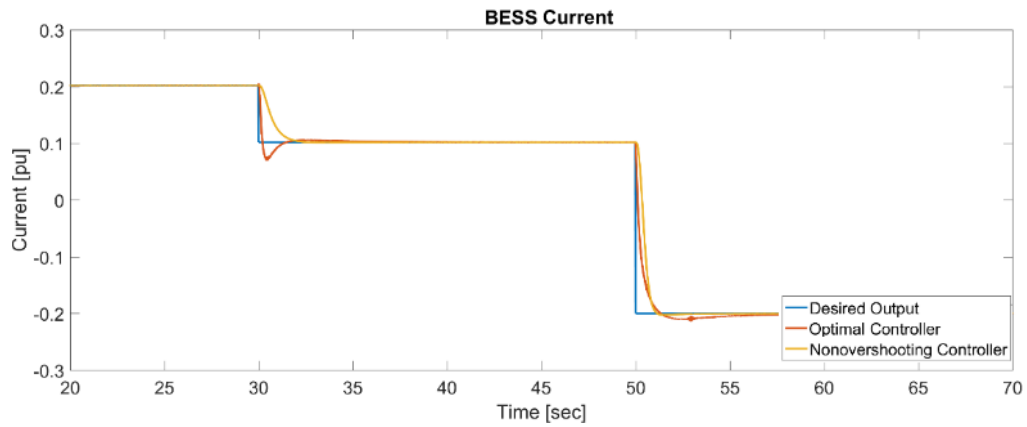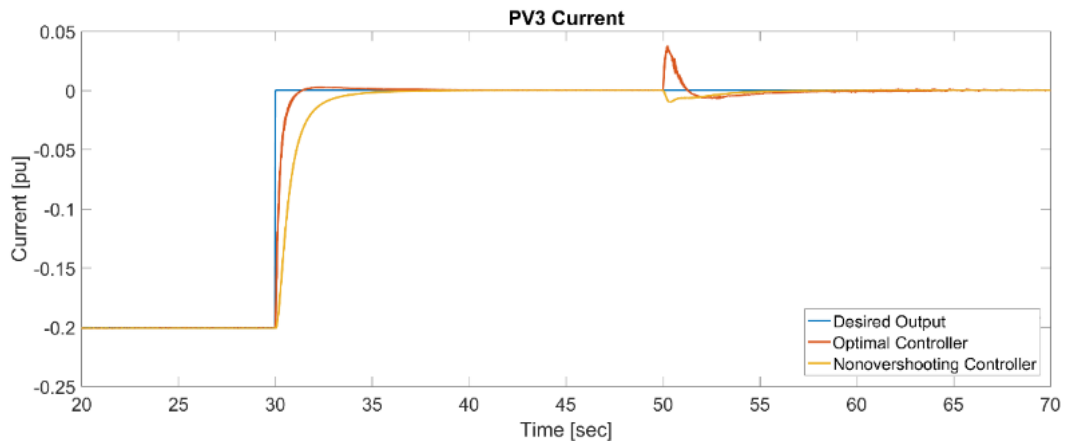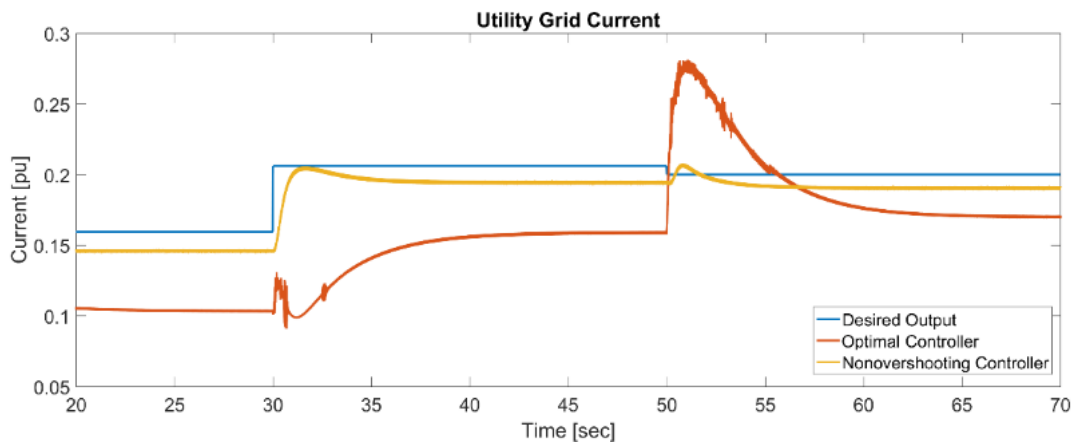
(a)
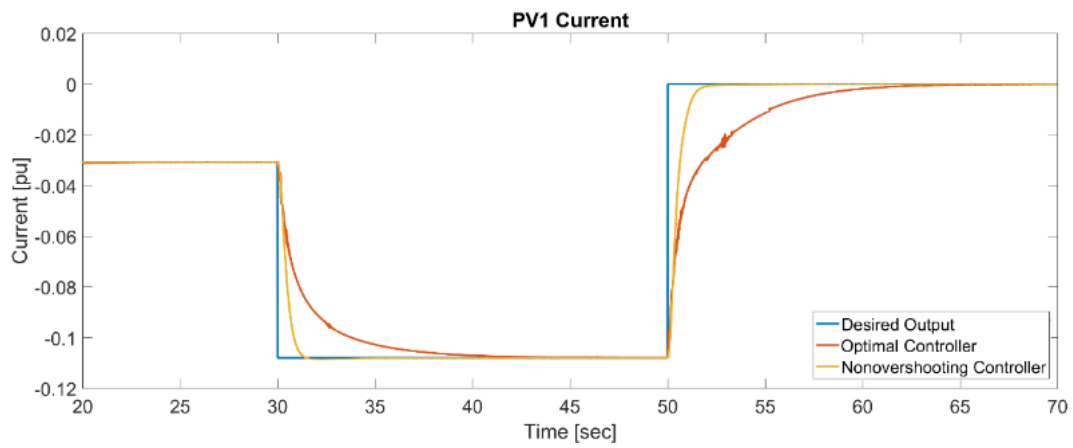
(b)
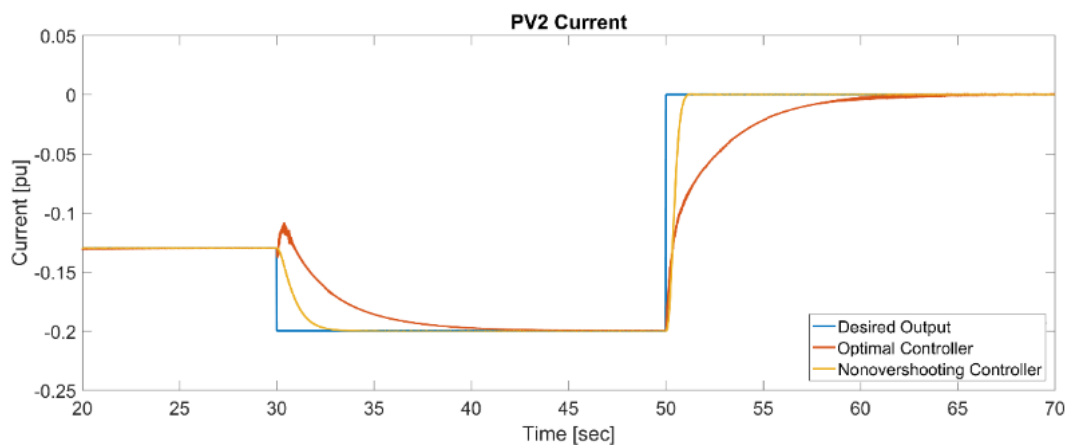
(c)

Figure 27. Current response using optimal controller and non-overshooting controller. (a)

BESS current (b) PV1 current (c) PV2 current.

(a)

(b)

Figure 28. Current response using optimal controller and non-overshooting controller. (a) PV3 current (b) UG current.
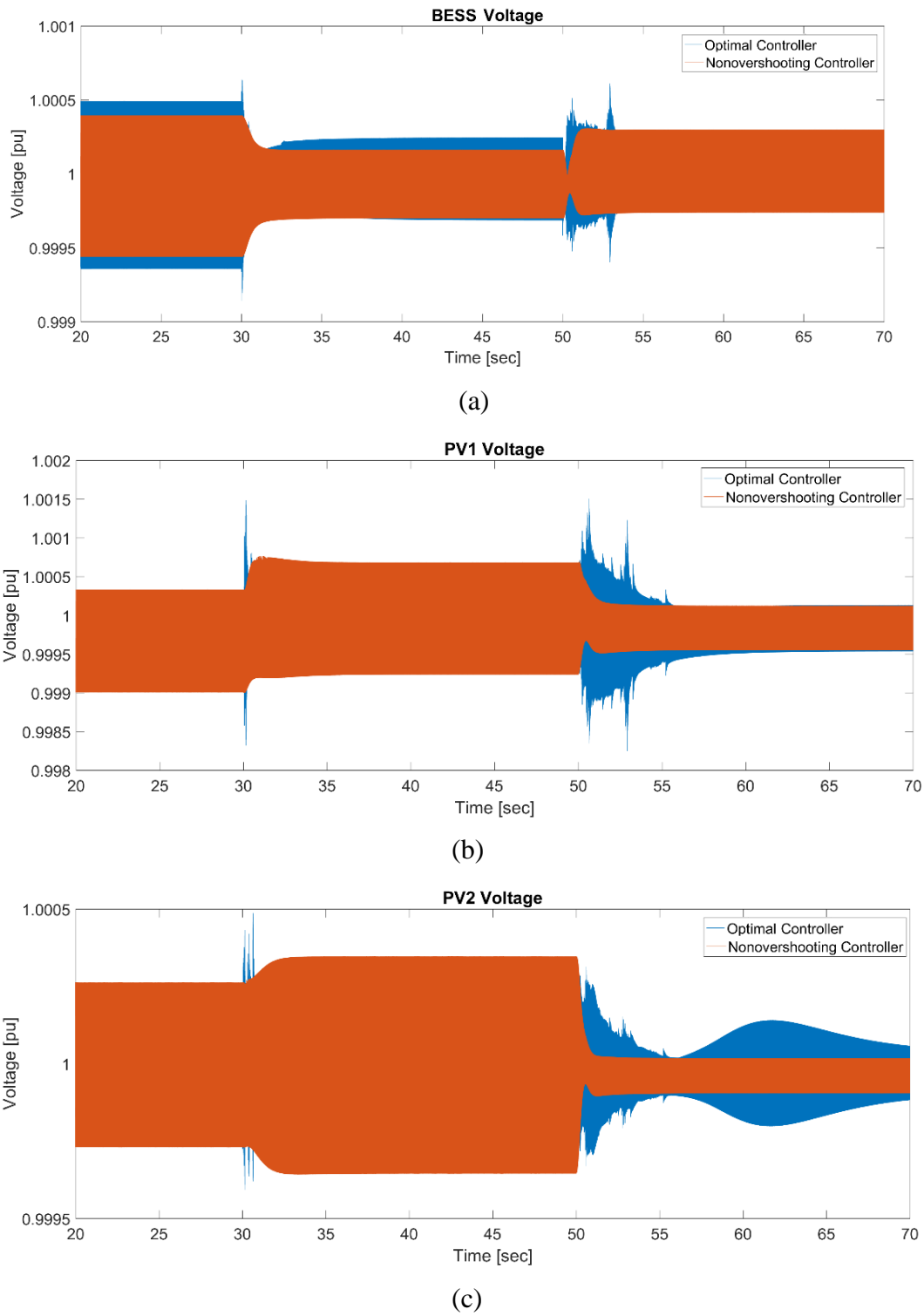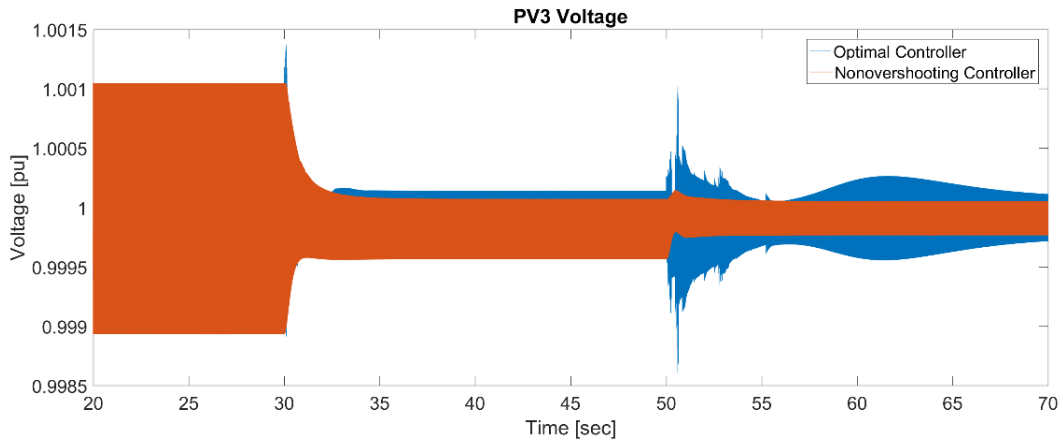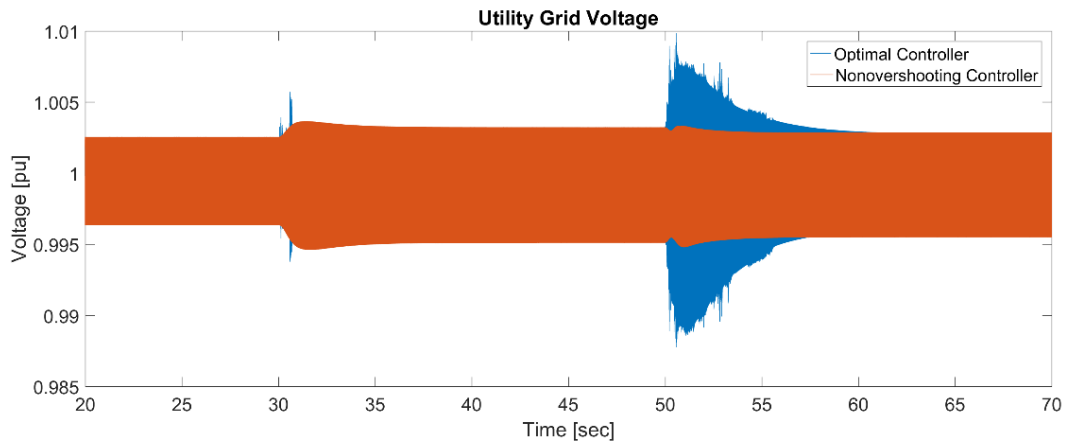
Figure 29. Voltage response using optimal controller and non-overshooting controller. (a)

BESS voltage (b) PV1 voltage (c) PV2 voltage.

(a)

(b)

Figure 30. Voltage response using optimal controller and non-overshooting controller. (a) PV3 voltage (b) UG voltage.

3.3 Summary

Two methods were used to obtain the feedback gain: the optimal control and the non-overshooting control methods. The flexibility of distributing selected modes among the output components when using the non-overshooting controller helped to attenuate the

overshoot response of the system. Both controllers were implemented to compare their responses when different operating modes were applied to the system. The voltage and current responses of the system illustrates how the non-overshooting controller has improved the overshot response compared to the optimal controller.

3.4 Fault Analysis for Multiport Converter

One of the main challenges of designing a multiport system is fault management. Faults in DC systems are considered to be extremely challenging due to the absence of zero-crossing in DC current, the high over-current and the fast transient that could lead to severe damages to the equipment [53, 54]. In order to design a reliable multiport converter, it is important to study the natural response of the system under fault condition. Generally, a fault in the multiport converter system goes through three main stages: pre-fault, during fault and post-fault stage. During these stages, the actions which are illustrated in Figure 31 occur [55]:
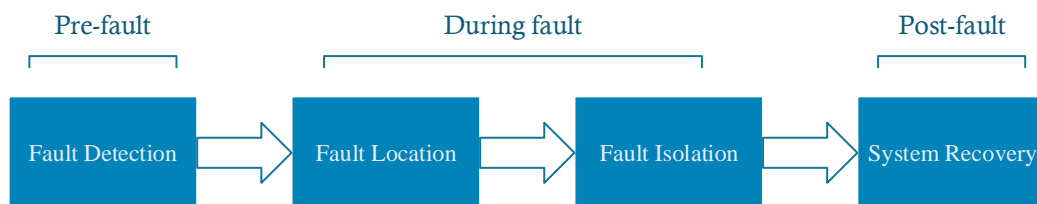

Figure 31. Fault stages in multiport converter system.

where each action is defined as follows:

- Fault Detection: Fault detection algorithm is used to detect any sudden overcurrent in the system.

- Fault Location: The faulted port is located, and a signal is sent to the circuit breaker (CB) connected to the faulted port.

- Fault isolation: The CB trips within a few milliseconds to isolate the faulted port before the fault propagates to other parts of the network.

- System Recovery: After isolating the fault, the system resumes its operation, and the output power of some of the ports are adjusted to compensate for the power loss caused by disconnecting the faulted port.

In this work, the main focus is to study the five-port converter's response in the post-fault stage where it is assumed that a fault has occurred at one of the ports and the CB has tripped and isolated the faulted port. This means that the state space model of the five-port converter that is used for designing the controller will change because the states and inputs related to the faulted port are removed. As a result, the system will operate as four-port converter system instead of five. Figure 32 illustrates the control structure used to analyze the fault response of the system. The switches are used to switch from the controller designed for the five-port system to the four-port system when a fault is injected to one of the ports. It is important to investigate the response of the system during this transition and the ability of the controller to ensure that the desired output is maintained. Two scenarios are simulated to study the voltage and current response of each port. In both scenarios, the aim is to ensure that the UG maintains constant power throughout the operation. In order to achieve this, the ports which are supplying the UG must be able to adjust their power output when the faulted port is isolated. Moreover, after injecting the fault in the system for a certain period of time, the fault is cleared, and the faulted port resumes its operation. The simulations are carried out using both the optimal and non-overshooting controllers to

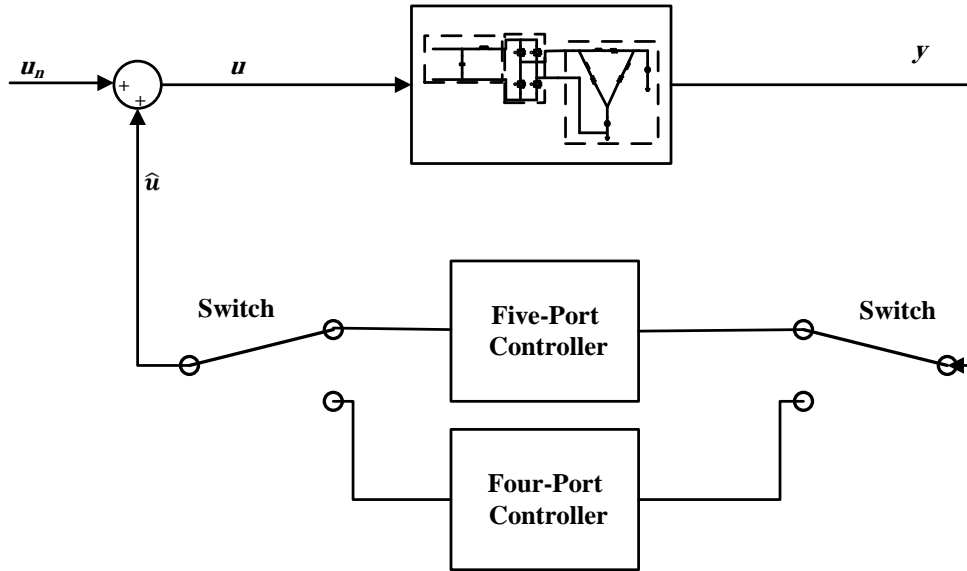compare the performance of the controllers.

*Figure 32*. Control structure for the system with two feedback controllers.

3.4.1 Simulation Result

In the first scenario, the fault is injected in one of the PV ports causing its CB to trip. The desired value during the pre-fault operation is set to [0.2019 -0.0308 -0.1298 -0.2009] which represent the BESS, PV1, PV2 and PV3 current respectively. The fault is injected at port 5 (PV3) at 20 sec, and the faulted port is isolated instantly as shown in Figures 33-34. It is noted that due to the isolation of port 5, the input power of the BESS is reduced and most of the output power from PVs is transferred to the UG in order to maintain the required power. The output current of PV3 goes to zero at 20 sec since it has been disconnected. The voltage is kept at 1 pu for all ports even after isolating the fault as shown in Figures 35-36. The fault lasts for 70 sec, and the faulted port is restored at 90

sec. Comparing the controller's transient performance in terms of overshoot, when the faulted port is isolated, the optimal controller provides better overshoot response for both current and voltage response for all ports except for PV1. The reason is that the non-overshooting controller was designed for the five-port converter and the four-port converter separately. As a result, when the fault is injected and the faulted port is removed, the switching from the five-port controller to the four-port controller causes the non-overshooting controller to not provide the desired performance. The controller was designed to operate for a specific system structure throughout the simulation. When the fault is cleared, and the faulted port is restored, the non-overshooting controller provides better overshoot response except for PV1. As for the settling time, the current and voltage responses show that using the non-overshooting controller; the current settles in less than 10 sec while it takes up to 80 sec for some of the port's current to settle using the optimal controller.
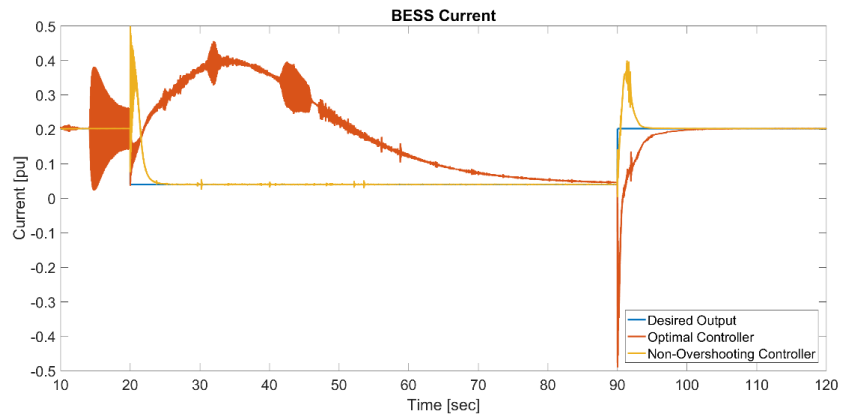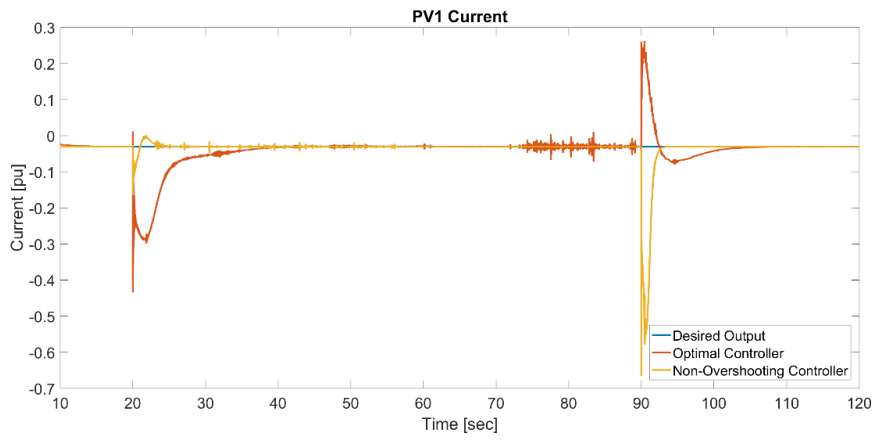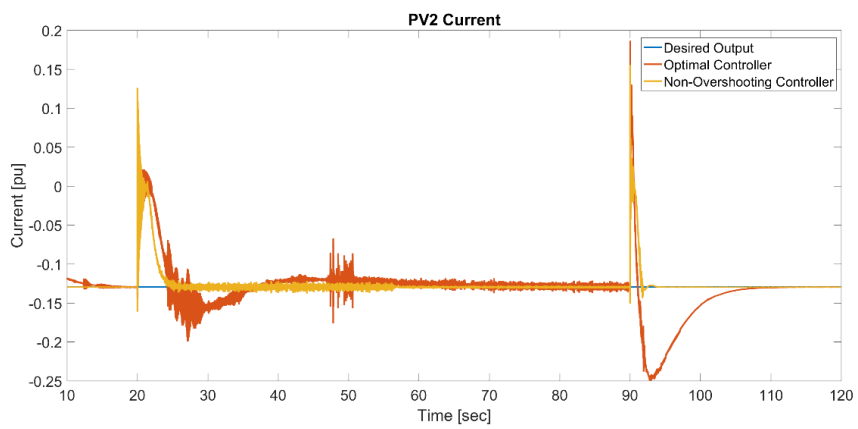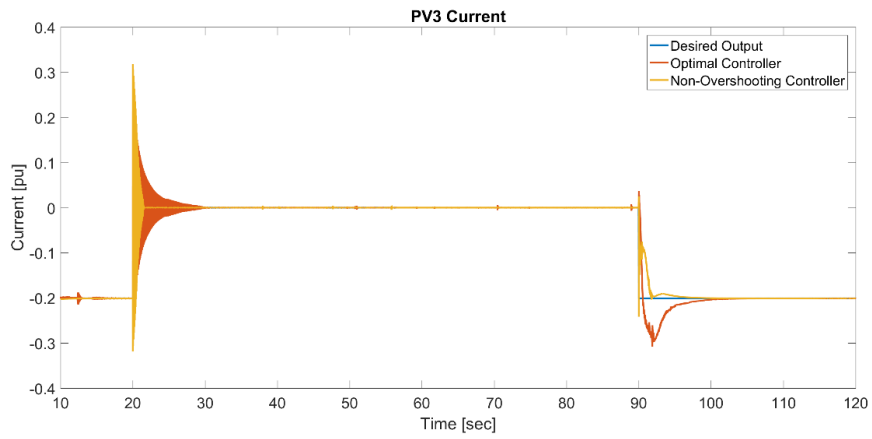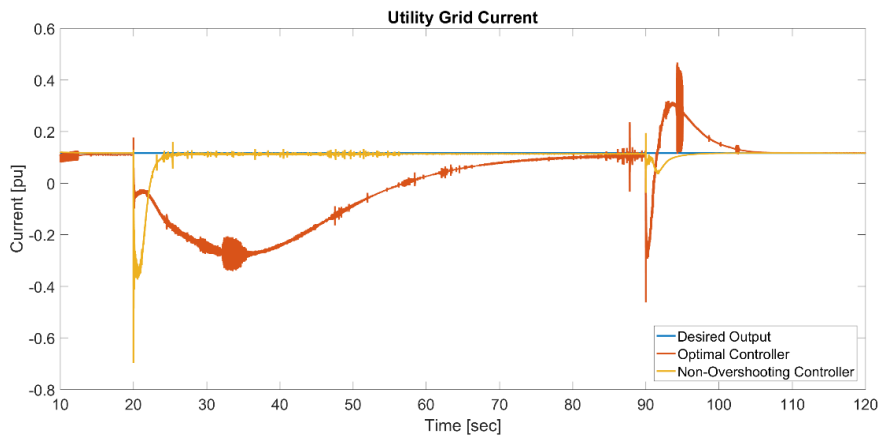
Figure 33. Current response to PV3 fault using optimal controller and non-overshooting

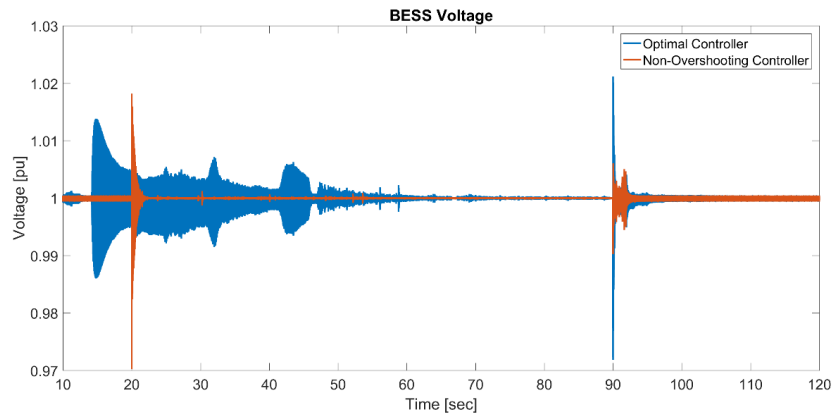controller. (a) BESS current (b) PV1 current (c) PV2 current.
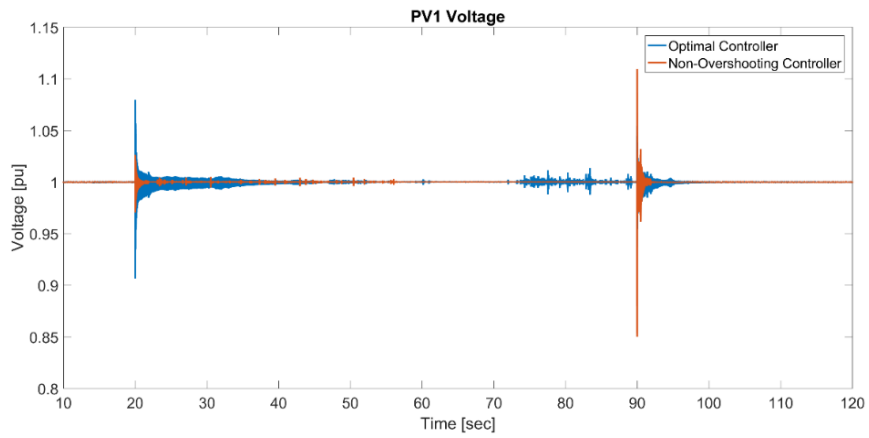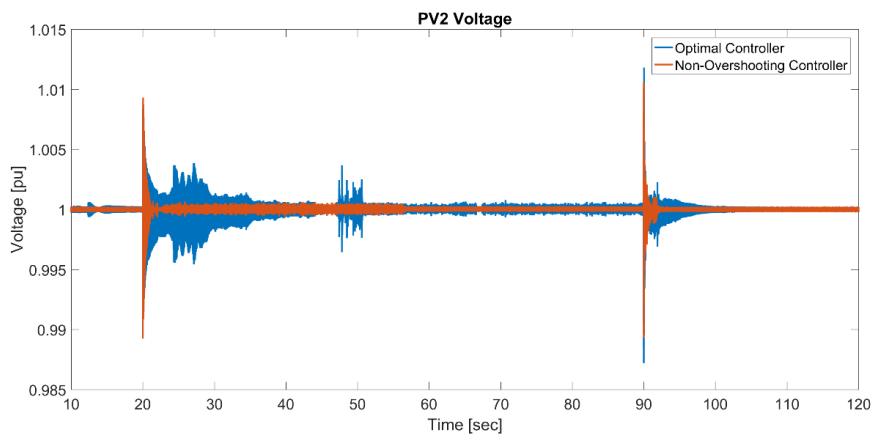
(a)

(b)

Figure 34. Current response to PV3 fault using optimal controller and non-overshooting controller. (a) PV3 current (b) UG current.

(a)

(b)

(c)

Figure 35. Voltage response to PV3 fault using optimal controller and non-overshooting

controller. (a) BESS voltage (b) PV1 voltage (c) PV2 voltage.
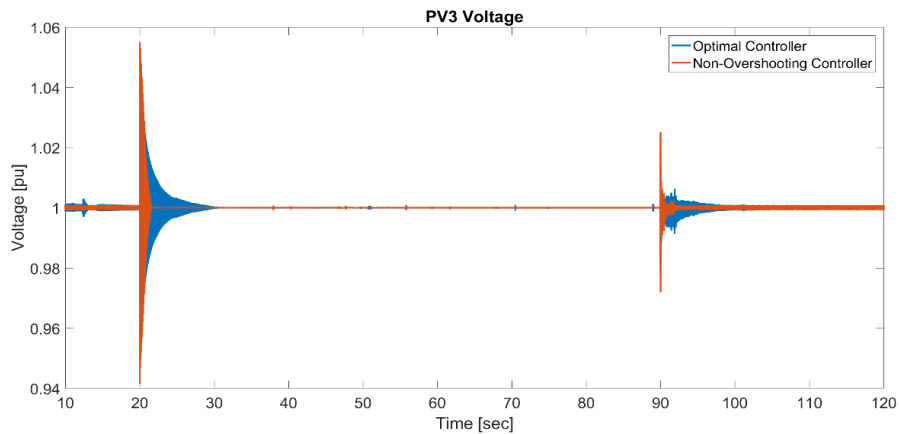
(a)
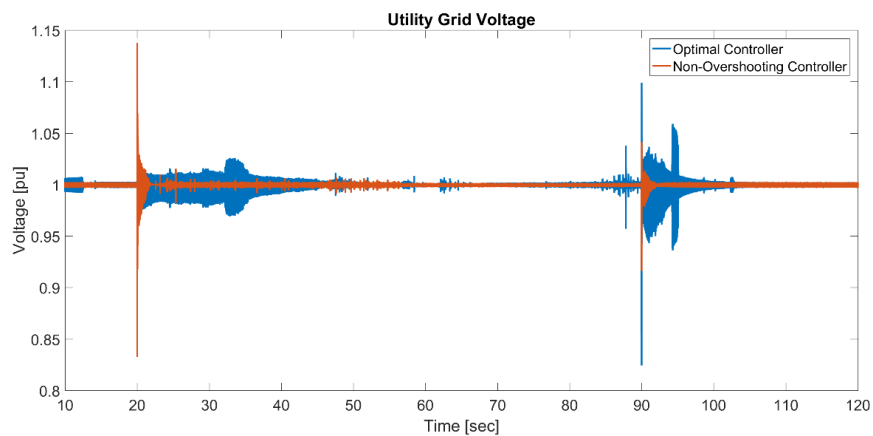
(b)

Figure *36*. Voltage response to PV3 fault using optimal controller and non-overshooting controller. (a) PV3 voltage (b) UG voltage.

In the second scenario, the fault is injected in BESS port at 20 sec, and the port is isolated. In the pre-fault operation, the output power of the PV ports is transferred to the BESS and the UG. Once the BESS port gets disconnected, all the generated power from the PV ports is transferred to the UG. The output power of the PV exceeds the amount required by the UG. As a result, the output current of the PV ports is adjusted as shown in

Figures 37-38 while keeping the voltage at 1 pu as shown in Figures 39-40. Although, both

controllers are able to maintain a constant supply to UG when the fault is injected, reducing

the PV current causes high noise to appear in the current and voltage response for PV2 and

PV3. The fault is cleared at 110 sec, and the port is restored. The non-overshooting

controller provides a quicker response than the optimal controller both at the time of

isolating the faulted port and once the port is restored.

(a)

(b)

Figure 37. Current response to BESS fault using optimal controller and non-overshooting

controller. (a) BESS current (b) PV1 current.
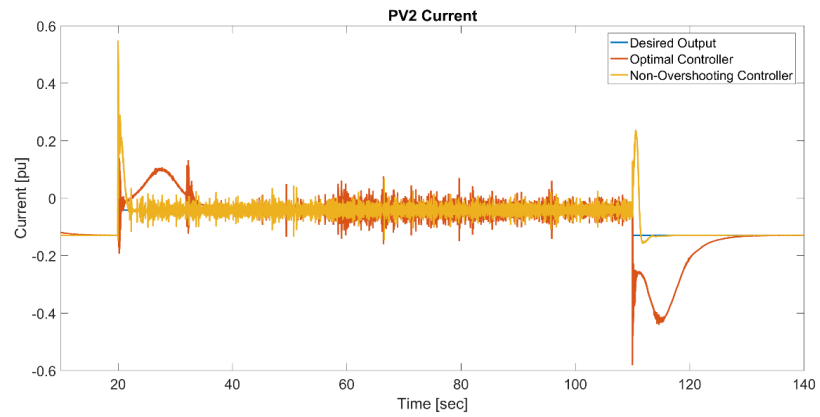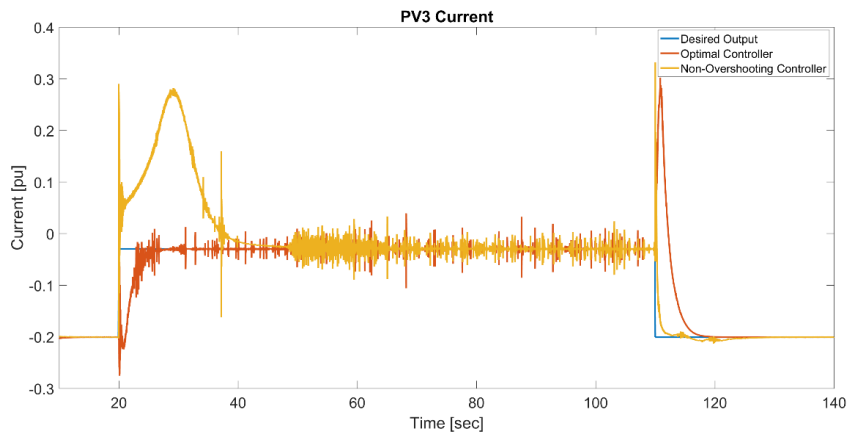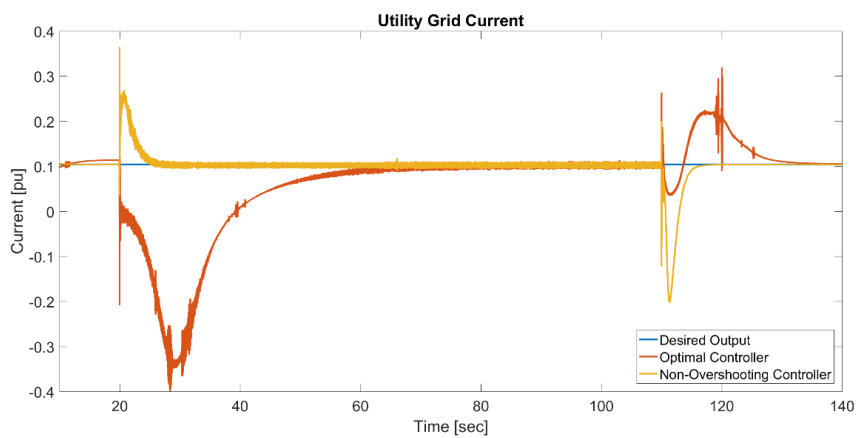
Figure 38. Current response to BESS fault using optimal controller and non-overshooting controller. (a) PV2 current (b) PV3 current (c) UG current.
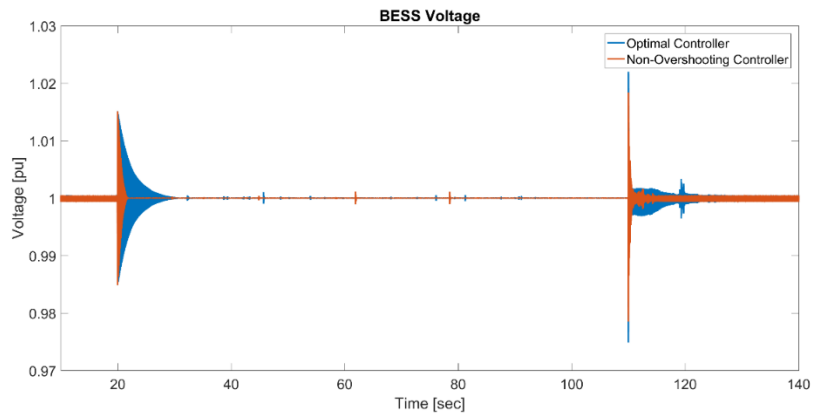
(a)
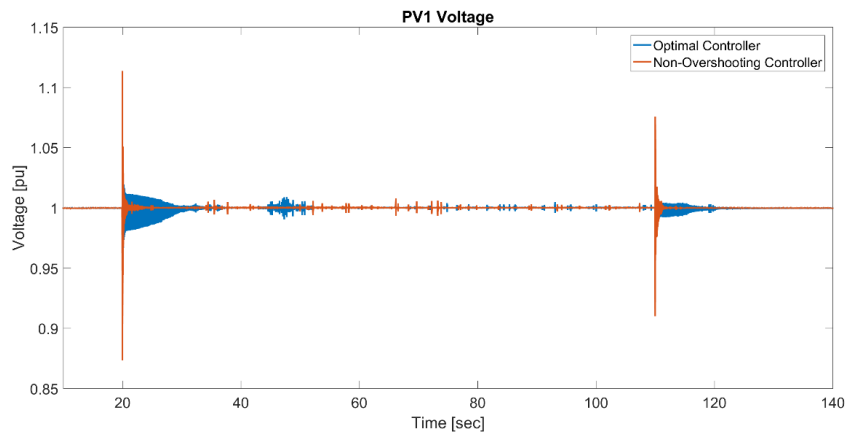
(b)
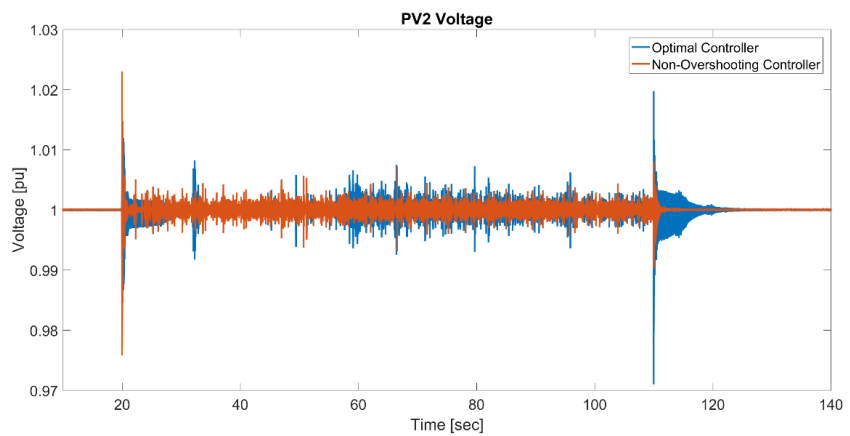
(c)

Figure 39. Voltage response to BESS fault using optimal controller and non-overshooting controller. (a) BESS voltage (b) PV1 voltage (c) PV2 voltage.
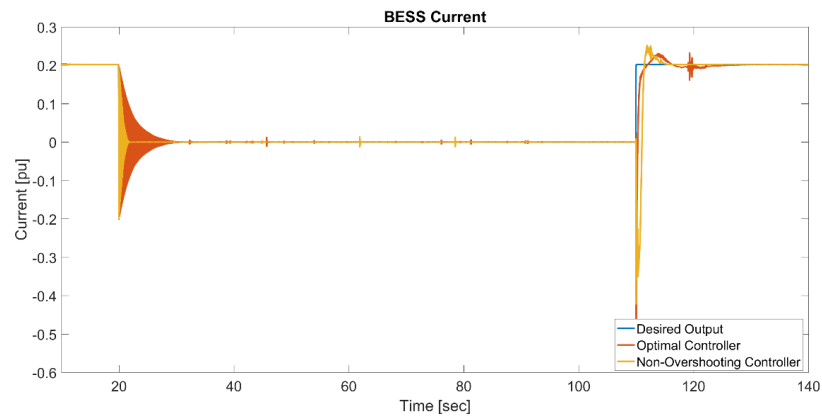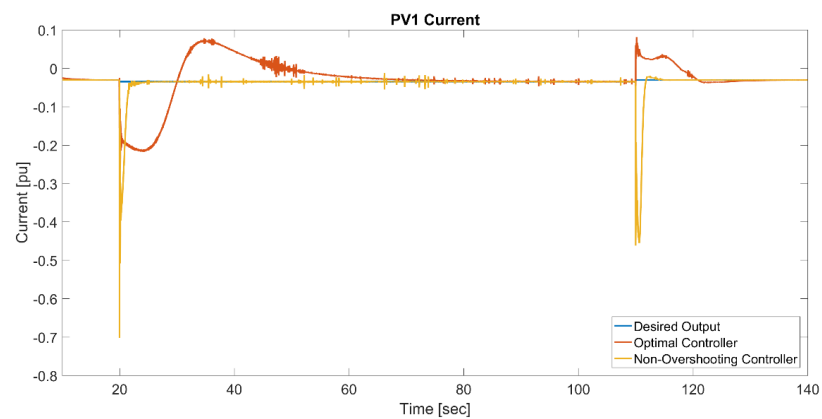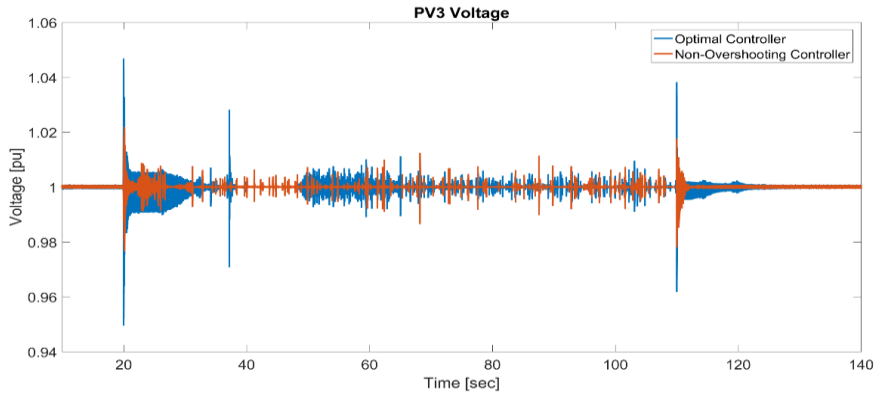
(a)
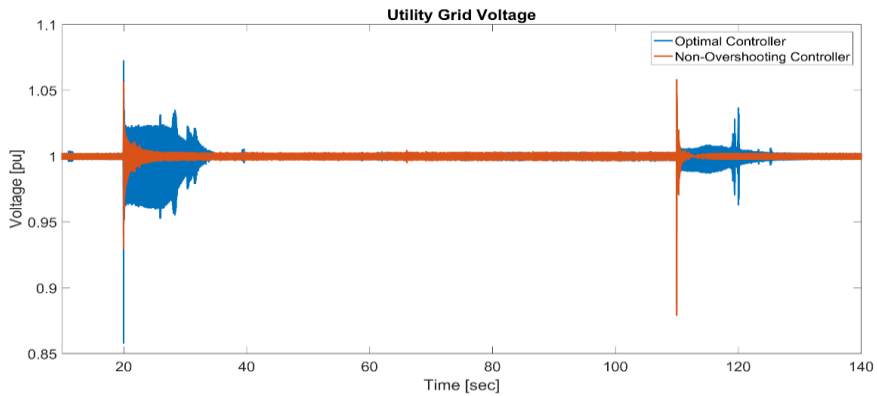
(b)

Figure 40. Voltage response to BESS fault using optimal controller and non-overshooting controller. (a) PV3 voltage (b) UG voltage.

3.5 Summary

This chapter presented the closed-loop control system used in the five-port converter. The state feedback gain was optimally assigned using LQR and a simulation was carried out for different operating condition to evaluate the controller response. The non-overshooting controller was then introduced to demonstrate its effect on enhancing the

overshoot response of the system. In addition, fault analysis was presented to evaluate the system ability to recover its operation when a fault is injected in the system. Two scenarios were simulated using the optimal controller and the non-overshooting controller and their response were compared.

CHAPTER 4: CONCLUSION AND FUTURE WORK

4.1 Conclusion

Due to the advancement in renewable energy technology, there comes a need for a system capable of interfacing multiple renewable energy sources with the connected loads. Using a single converter for each source has proven to increase the cost and reduce the reliability and the efficiency of the system. This has led to the development of a multi-input multi-output converter capable of integrating multiple renewable energy sources and control the power transfer using a centralized controller. Several topologies of high-power multiport converter were presented in the literature. The converters are classified based on their power capability, support for bidirectional power flow and the support for adding additional ports. This thesis focuses on analyzing high-power DAB based multiport converter to interface utility grid, battery energy storage system, and three PVs.

A generalized average current equation was derived for the DAB converter and used to obtain the average power equation. The equivalent circuit for each port was presented and used to develop large and small signal models. In addition, the detailed model which takes into account the losses associated with the winding resistance and the switching action was developed. In order to attenuate the harmonics generated by the switches, a simple LC filter was designed, and a mathematical equation was derived for obtaining the minimum L and C based on the required voltage and current ripples.

State feedback controller scheme was developed in order to ensure stable operation of the system. First, an optimal controller was designed using LQR, and simulation was carried out to validate the controller response. It was noted that the transient response of the current and voltage suffer from high overshoot and settling time. To overcome this, a

non-overshooting controller was designed and simulated to compare its performance with the optimal controller. It was shown that the non-overshooting controller was able to enhance the overshoot response and the settling time of the current and voltage responses. Finally, fault analysis was performed to asses the system response under fault. The fault was injected in the PV port and the BESS port, and the current and voltage responses were analyzed. It was found that the non-overshooting controller did not perform well in terms of reducing the overshoot. The reason for that is when a fault is injected to the five-port system, and the faulted port gets isolated, the feedback loop switches from the controller that was designed for five-port converter to the four-port converter. Although the non-overshooting controller was not designed for such cases, it was able to provide much quicker response than the optimal controller.

4.2 Future Work

The practical implementation of the proposed converter can be investigated to validate the system response using the proposed controllers under different operating condition. In addition, the selection of the power semiconductor device and the losses associated with the switching action can be further studied. Moreover, this work can be extended by developing maximum power tracking technique using the centralized controller to extract the maximum power from the connected PVs. The implementation of the proposed converter in other applications such as electric vehicles can be also investigated. The fault analysis of the multiport converter can be extended by studying the type of faults that could affect the system and the protection scheme needed to protect the system from such faults.

REFERENCES

[1]   U. E. I. Administration, "International Energy Outlook 2017," 2017.

[2]   REN21, "Renewables 2017 Global Status Report," Paris, France978-3-9818107-
        6-9, 2017.

[3]   T. Kerekes, E. Koutroulis, D. Séra, R. Teodorescu, and M. Katsanevakis, "An
        Optimization Method for Designing Large PV Plants," *IEEE Journal of
        Photovoltaics,* vol. 3, no. 2, pp. 814-822, 2013.

[4]   Z. Chen, Q. Zhou, and J. Xu, "Coupled-inductor boost integrated flyback
        converter with high-voltage gain and ripple-free input current," *IET Power
        Electronics,* vol. 8, no. 2, pp. 213-220, 2015.

[5]   Y. P. Siwakoti, F. Blaabjerg, P. C. Loh, and G. E. Town, "High-voltage boost
        quasi-Z-source isolated DC/DC converter," *IET Power Electronics,* vol. 7, no. 9,
        pp. 2387-2395, 2014.

[6]   U. R. P and A. K. Rathore, "Extended Range ZVS Active-Clamped Current-Fed
        Full-Bridge Isolated DC/DC Converter for Fuel Cell Applications: Analysis,
        Design, and Experimental Results," *IEEE Transactions on Industrial Electronics,*
        vol. 60, no. 7, pp. 2661-2672, 2013.

[7]   H. Tao, A. Kotsopoulos, J. L. Duarte, and M. A. M. Hendrix, "Family of
        multiport bidirectional DC-DC converters," *IEE Proceedings - Electric Power
        Applications,* vol. 153, no. 3, pp. 451-458, 2006.

[8]   C. Yaow-Ming, L. Yuan-Chuan, and W. Feng-Yu, "Multi-input DC/DC converter
        based on the multiwinding transformer for renewable energy applications," *IEEE
        Transactions on Industry Applications,* vol. 38, no. 4, pp. 1096-1104, 2002.

[9]   H. Wu, J. Zhang, and Y. Xing, "A Family of Multiport Buck-Boost Converters Based on DC-Link-Inductors (DLIs)," *IEEE Transactions on Power Electronics,* vol. 30, no. 2, pp. 735-746, 2015.

[10]   K. Gummi and M. Ferdowsi, "Double-Input DC-DC Power Electronic Converters for Electric-Drive Vehicles Topology Exploration and Synthesis Using a Single-Pole Triple-Throw Switch," *IEEE Transactions on Industrial Electronics,* vol. 57, no. 2, pp. 617-623, 2010.

[11]   K. P. Yalamanchili, M. Ferdowsi, and K. Corzine, "New Double Input DC-DC Converters for Automotive Applications," in *2006 IEEE Vehicle Power and Propulsion Conference*, Windsor, UK, 2006, pp. 1-6.

[12]   Y. Yuan-mao and K. W. E. Cheng, "Multi-input voltage-summation converter based on switched-capacitor," *IET Power Electronics,* vol. 6, no. 9, pp. 1909-1916, 2013.

[13]   K. Gummi and M. Ferdowsi, "Derivation of new double-input DC-DC converters using H-Bridge cells as building blocks," in *2008 34th Annual Conference of IEEE Industrial Electronics*, Orlando, FL, USA, 2008, pp. 2806-2811.

[14]   H. Behjati and A. Davoudi, "A Multiple-Input Multiple-Output DC-DC Converter," *IEEE Transactions on Industry Applications,* vol. 49, no. 3, pp. 1464-1479, 2013.

[15]   H. Tao, A. Kotsopoulos, J. L. Duarte, and M. A. M. Hendrix, "Multi-input bidirectional DC-DC converter combining DC-link and magnetic-coupling for fuel cell systems," in *Fourtieth IAS Annual Meeting. Conference Record of the*

2005 Industry Applications Conference, 2005., Kowloon, Hong Kong, China, 2005, vol. 3, pp. 2021-2028 Vol. 3.

[16]   H. Al-Atrash and I. Batarseh, "Boost-Integrated Phase-Shift Full-Bridge Converter for Three-Port Interface," in *2007 IEEE Power Electronics Specialists Conference*, Orlando, FL, USA, 2007, pp. 2313-2321.

[17]   M. N. Kheraluwala, R. W. Gascoigne, D. M. Divan, and E. D. Baumann, "Performance characterization of a high-power dual active bridge DC-to-DC converter," *IEEE Transactions on Industry Applications,* vol. 28, no. 6, pp. 1294-1301, 1992.

[18]   H. Krishnaswami and N. Mohan, "Constant switching frequency series resonant three-port bi-directional DC-DC converter," in *2008 IEEE Power Electronics Specialists Conference*, Rhodes, Greece, 2008, pp. 1640-1645.

[19]   H. Tao, A. Kotsopoulos, J. L. Duarte, and M. A. M. Hendrix, "A Soft-Switched Three-Port Bidirectional Converter for Fuel Cell and Supercapacitor Applications," in *2005 IEEE 36th Power Electronics Specialists Conference*, Recife, Brazil, 2005, pp. 2487-2493.

[20]   N. F. P. Association, *National Electrical Code*. USA: National Fire Protection Association, 2016, p. 820.

[21]   R. Gonzalez, E. Gubia, J. Lopez, and L. Marroyo, "Transformerless Single-Phase Multilevel-Based Photovoltaic Inverter," *IEEE Transactions on Industrial Electronics,* vol. 55, no. 7, pp. 2694-2702, 2008.

[22] A. M. Ari, "Modeling, analysis, and control of multi-port DC-DC converters," Doctor of Philosophy, Purdue University, ProQuest Dissertations Publishing, 2014.

[23] R. W. A. A. D. Doncker, D. M. Divan, and M. H. Kheraluwala, "A three-phase soft-switched high-power-density DC/DC converter for high-power applications," *IEEE Transactions on Industry Applications,* vol. 27, no. 1, pp. 63-73, 1991.

[24] A. M. Ari, L. Li, and O. Wasynczuk, "Control and Optimization of N-Port DC-DC Converters," *IEEE Transactions on Control Systems Technology,* vol. 24, no. 4, pp. 1521-1528, 2016.

[25] A. M. Ari, L. Li, and O. Wasynczuk, "Modeling and analysis of N-port DC-DC converters using the cyclic average current," in *2012 Twenty-Seventh Annual IEEE Applied Power Electronics Conference and Exposition (APEC)*, Orlando, FL, USA, 2012, pp. 863-869.

[26] M. Erdei, "Multiwinding ideal transformers as multiport components," *Electronics Letters,* vol. 1, no. 7, pp. 197-199, 1965.

[27] D. Morris, "Some practical equivalent circuits for multi-circuit transformers," *Proceedings of the IEE - Part II: Power Engineering,* vol. 98, no. 62, pp. 256-261, 1951.

[28] V. A. Niemela, H. A. Owen, and T. G. Wilson, "Cross-coupled-secondaries model for multiwinding transformers with parameter values calculated from short-circuit impedances," in *21st Annual IEEE Conference on Power Electronics Specialists*, San Antonio, TX, USA, 1990, pp. 822-830.

[29] C. Qing, F. C. Lee, J. Jian Zhong, and M. M. Jovanovic, "A new model for multiple-winding transformer," in *Proceedings of 1994 Power Electronics Specialist Conference - PESC'94*, Taipei, Taiwan, Taiwan, 1994, vol. 2, pp. 864-871 vol.2.

[30] A. Davoudi and J. Jatskevich, "Realization of parasitics in state-space average-value modeling of PWM DC-DC converters," *IEEE Transactions on Power Electronics,* vol. 21, no. 4, pp. 1142-1147, 2006.

[31] K. Zhang, Z. Shan, and J. Jatskevich, "Large- and Small-Signal Average-Value Modeling of Dual-Active-Bridge DC-DC Converter Considering Power Losses," *IEEE Transactions on Power Electronics,* vol. 32, no. 3, pp. 1964-1974, 2017.

[32] S. Chiniforoosh *et al.*, "Definitions and Applications of Dynamic Average Models for Analysis of Power Systems," *IEEE Transactions on Power Delivery,* vol. 25, no. 4, pp. 2655-2669, 2010.

[33] N. V. P and M. K. Kazimierczuk, "Small-Signal Modeling of Open-Loop PWM Z-Source Converter by Circuit-Averaging Technique," *IEEE Transactions on Power Electronics,* vol. 28, no. 3, pp. 1286-1296, 2013.

[34] A. Davoudi, J. Jatskevich, and T. D. Rybel, "Numerical state-space average-value modeling of PWM DC-DC converters operating in DCM and CCM," *IEEE Transactions on Power Electronics,* vol. 21, no. 4, pp. 1003-1012, 2006.

[35] C. Yaow-Ming and L. Yuan-Chuan, "Development of multi-port converters for hybrid wind-photovoltaic power system," in *Proceedings of IEEE Region 10 International Conference on Electrical and Electronic Technology. TENCON 2001 (Cat. No.01CH37239)*, Singapore, 2001, vol. 2, pp. 804-808 vol.2.

[36] H. K. Krishnamurthy and R. Ayyanar, "Building Block Converter Module for Universal (AC-DC, DC-AC, DC-DC) Fully Modular Power Conversion Architecture," in *2007 IEEE Power Electronics Specialists Conference*, Orlando, FL, USA, 2007, pp. 483-489.

[37] M. Santhi, "Dynamic analysis of multi-output push-pull ZCS-quasi resonant converter," in *2007 IET-UK International Conference on Information and Communication Technology in Electrical Sciences (ICTES 2007)*, Tamil Nadu, India, 2007, pp. 229-237.

[38] V. Grigore, J. Hatonen, J. Kyyra, and T. Suntio, "Dynamics of a buck converter with a constant power load," in *PESC 98 Record. 29th Annual IEEE Power Electronics Specialists Conference (Cat. No.98CH36196)*, Fukuoka, Japan, 1998, vol. 1, pp. 72-78 vol.1.

[39] A. Rosen, "A new network theorem," *Electrical Engineers, Journal of the Institution of,* vol. 62, no. 335, pp. 916-918, 1924.

[40] R. W. E. a. D. Maksimovic, *Fundamentals of Power Electronics*. USA: Springer US, 2001, p. 883.

[41] "DC–DC Power Converters," in *Wiley Encyclopedia of Electrical and Electronics Engineering*.

[42] A. M. Ari, L. Li, and O. Wasynczuk, "Filter design for N-port DC-DC converters," in *2013 IEEE Power and Energy Conference at Illinois (PECI)*, Champaign, IL, USA, 2013, pp. 135-141.

[43] C. W. T. McLyman, *Transformer and Inductor Design Handbook*. Boca Raton: CRC Press, 2004, p. 556.

[44] M. F. S. a. G. C. V. John G. Kassakian, *Principles of Power Electronics*. Pearson 1991, p. 740.

[45] S. Oucheriah and L. Guo, "PWM-Based Adaptive Sliding-Mode Control for Boost DC–DC Converters," *IEEE Transactions on Industrial Electronics,* vol. 60, no. 8, pp. 3291-3294, 2013.

[46] M. M. Peretz and S. Ben-Yaakov, "Time-Domain Design of Digital Compensators for PWM DC-DC Converters," *IEEE Transactions on Power Electronics,* vol. 27, no. 1, pp. 284-293, 2012.

[47] D. Czarkowski, L. R. Pujara, and M. K. Kazimierczuk, "Robust stability of state-feedback control of PWM DC-DC push-pull converter," *IEEE Transactions on Industrial Electronics,* vol. 42, no. 1, pp. 108-111, 1995.

[48] J. Alvarez-Ramirez, I. Cervantes, G. Espinosa-Perez, P. Maya, and A. Morales, "A stable design of PI control for DC-DC converters with an RHS zero," *IEEE Transactions on Circuits and Systems I: Fundamental Theory and Applications,* vol. 48, no. 1, pp. 103-106, 2001.

[49] R. Schmid and L. Ntogramatzidis, "A unified method for the design of nonovershooting linear multivariable state-feedback tracking controllers," *Automatica,* vol. 46, no. 2, pp. 312-321, 2010/02/01/ 2010.

[50] G. F. Franklin, D. J. Powell, and A. Emami-Naeini, *Feedback Control of Dynamic Systems*. Prentice Hall PTR, 2001, p. 912.

[51] F. H. F. Leung, P. K. S. Tam, and C. K. Li, "The control of switching DC-DC converters-a general LWR problem," *IEEE Transactions on Industrial Electronics,* vol. 38, no. 1, pp. 65-71, 1991.

[52]   B. Moore, "On the flexibility offered by state feedback in multivariable systems
        beyond closed loop eigenvalue assignment," *IEEE Transactions on Automatic
        Control,* vol. 21, no. 5, pp. 689-692, 1976.

[53]   B. Geebelen, W. Leterme, and D. V. Hertem, "Analysis of DC breaker
        requirements for different HVDC grid protection schemes," in *11th IET
        International Conference on AC and DC Power Transmission*, Birmingham, UK,
        2015, pp. 1-7.

[54]   E. Kontos, R. T. Pinto, S. Rodrigues, and P. Bauer, "Impact of HVDC
        Transmission System Topology on Multiterminal DC Network Faults," *IEEE
        Transactions on Power Delivery,* vol. 30, no. 2, pp. 844-852, 2015.

[55]   P. Wang, "A Multi-Terminal Modular Multilevel Converter-Based HVDC System
        With An Offshore Wind Farm," Doctor of Philosophy, School of Electronic, The
        University of Birmingham, 2015.